

Modeling channelized and distributed subglacial drainage in two dimensions

Mauro A. Werder,^{1,2} Ian J. Hewitt,^{3,4} Christian G. Schoof,⁵ and Gwenn E. Flowers¹

Received 5 March 2013; revised 9 September 2013; accepted 13 September 2013.

[1] We present a two-dimensional Glacier Drainage System model (GlaDS) that couples distributed and channelized subglacial water flow. Distributed flow occurs through linked cavities that are represented as a continuous water sheet of variable thickness. Channelized flow occurs through R othlisberger channels that can form on any of the edges of a prescribed, unstructured network of potential channels. Water storage is accounted for in an englacial aquifer and in moulins, which also act as point sources of water to the subglacial system. Solutions are presented for a synthetic topography designed to mimic an ice sheet margin. For low discharge, all the flow is accommodated in the sheet, whereas for sufficiently high discharge, the model exhibits a channelization instability which leads to the formation of a self-organized channel system. The random orientation of the network edges allows the channel system geometry to be relatively unbiased, in contrast to previous structured grid-based models. Under steady conditions, the model supports the classical view of the subglacial drainage system, with low pressure regions forming around the channels. Under diurnally varying input, water flows in and out of the channels, and a rather complex spatiotemporal pattern of water pressures is predicted. We explore the effects of parameter variations on the channel system topology and mean effective pressure. The model is then applied to a mountain glacier and forced with meltwater calculated by a temperature index model. The results are broadly consistent with our current understanding of the glacier drainage system and demonstrate the applicability of the model to real settings.

Citation: Werder, M. A., I. J. Hewitt, C. G. Schoof, and G. E. Flowers (2013), Modeling channelized and distributed subglacial drainage in two dimensions, *J. Geophys. Res. Earth Surf.*, 118, doi:10.1002/jgrf.20146.

1. Introduction

[2] Water movement beneath glaciers and ice sheets is important because of its influence on ice flow [e.g., *Iken and Bindshadler*, 1986; *Kamb*, 1987], its contribution to glacial erosion [e.g., *Iverson*, 2012], to catchment hydrology, subglacial biology [e.g., *Siegert et al.*, 2001], and because of the hazard potential of glacier outburst floods [e.g., *Nye*, 1976]. Renewed interest has been generated recently by the still poorly understood link between surface melt and ice sheet

dynamics [e.g., *Joughin et al.*, 2008] and its implications for future sea level rise [*IPCC*, 2007]. In particular, recent observations of the Greenland Ice Sheet suggest that meltwater produced on the ice surface can significantly alter the speed at which the ice moves [e.g., *Hoffman et al.*, 2011; *Bartholomew et al.*, 2012].

[3] Where it occurs, surface melting is usually the predominant source of water, whereas meltwater fluxes produced by geothermal or frictional heating at the bed are typically orders of magnitude smaller. Our attention is focused primarily on this situation, which is relevant for most alpine glaciers as well as for the margins of the Greenland Ice Sheet. Surface meltwater typically collects into streams before disappearing into crevasses or moulins. It is transported englacially in channels and fractures and eventually reaches the bed, where it flows through a subglacial drainage system to the terminus, often reemerging in a single or few streams [see *Fountain and Walder*, 1998, and references therein].

[4] The subglacial drainage system appears to exert a key control on ice dynamics, as well as being central to other aspects of glacial hydrology. Particularly important is the distinction between two broad categorizations of the drainage system: a slow, distributed system and a fast, channelized system, which forms during periods of high

Additional supporting information may be found in the online version of this article.

¹Department of Earth Sciences, Simon Fraser University, Burnaby, British Columbia, Canada.

²Now at School of Geographical Sciences, University of Bristol, Bristol, UK.

³Department of Mathematics, University of British Columbia, Vancouver, British Columbia, Canada.

⁴Now at Mathematical Institute, University of Oxford, Oxford, UK.

⁵Department of Earth and Ocean Sciences, University of British Columbia, Vancouver, British Columbia, Canada.

Corresponding author: M. A. Werder, School of Geographical Sciences, University of Bristol, University Road, Bristol BS8 1SS, UK. (m.a.werder@bristol.ac.uk)

discharge. The distributed system may comprise flow between cavities that open behind bedrock bumps due to ice sliding, a so-called “linked cavity system” [Walder, 1986; Kamb, 1987], a water sheet of more or less uniform thickness [Weertman, 1972; Flowers and Clarke, 2002; Creyts and Schoof, 2009], as well as permeable subglacial till [Shoemaker, 1986]. Channelized drainage occurs most commonly through conduits melted into the base of the ice, known as *Röthlisberger (R) channels* [Röthlisberger, 1972; Nye, 1976]. Channels may also be incised into the bedrock or sediments [Nye, 1973; Walder and Fowler, 1994; Ng, 2000]. Both distributed and channelized systems may be possible whether the glacier bed is hard, i.e., bedrock, or soft, i.e., sediments.

[5] The goal of this work is to integrate both distributed and channelized drainage in a two-dimensional (2-D) model. Most previous models that combine both drainage mechanisms have been zero-dimensional “box” models [Clarke, 1996] or one-dimensional “flow-line” models. For example, Flowers *et al.* [2004] combined a distributed water sheet in parallel with a series of channels, and Kessler and Anderson [2004] described discrete drainage pathways that comprise a mixture of cavities and channels, allowing a transition between distributed and channelized modes.

[6] On the other hand, most previous 2-D models include only a distributed component [e.g., Flowers and Clarke, 2002; Johnson and Fastook, 2002; Le Brocq *et al.*, 2009]. Arnold and Sharp [2002] used a model that incorporates both distributed and channel flow, but assumed a steady state in which only one or the other operates. More recently, Schoof [2010] presented a 2-D network of discrete conduits that could behave as both channels and cavities. The individual conduits in the model are similar to the ones in Kessler and Anderson [2004] and to those originally proposed by Walder [1986]. Schoof’s [2010] treatment allows for the formation of an arborescent channel system when the discharge is sufficiently large. However, the computations were done only on a rectangular grid of individual conduits, which strongly affects the morphology of the arborescent drainage system that emerges. For practical simulations, this discrete approach is hampered by the need to resolve individual flow paths of the distributed system, which we expect to be on a scale of meters. A different approach to represent the distributed system was used by Creyts and Schoof [2009] who described flow through a sheet of water with the ice roof supported by rock clasts of different sizes. A mathematically similar model was presented by Hewitt [2011] who used a water sheet to represent many evolving linked cavities averaged over a suitably large patch of the bed that were coupled to a single channel. A recent study by Hewitt [2013] has integrated such a linked-cavity sheet with a structured channel network (similar to Schoof’s [2010] approach) to investigate the coupling with ice dynamics. The two papers, Schoof *et al.* [2012] and Hewitt *et al.* [2012], introduced a coupled channel and sheet model with the added complication of free surface flow at atmospheric pressure and ice uplift due to hydraulic jacking. However, their numerics only addressed the one-dimensional problem.

[7] The glacier drainage system model GlaDS presented in this paper combines water flow through a sheet, derived as averaged linked cavities, with flow through a network of conduits that lie on an unstructured numerical mesh. It

Table 1. Parameters and Values Used in Synthetic Model Runs^a

Description	Symbol	Value	Units
Acceleration due to gravity	g	9.81	m s^{-2}
Latent heat	L	3.34×10^5	J kg^{-1}
Ice density	ρ_i	910	kg m^{-3}
Water density	ρ_w	1000	kg m^{-3}
Pressure melt coefficient	c_i	7.5×10^{-8}	K Pa^{-1}
Heat capacity of water	c_w	4.22×10^3	$\text{J kg}^{-1} \text{K}^{-1}$
First sheet flow exponent	α	5/4	
Second sheet flow exponent	β	3/2	
First channel flow exponent	α_c	5/4	
Second channel flow exponent	β_c	3/2	
Sheet conductivity ^b	k	0.01	$\text{m}^{7/4} \text{kg}^{-1/2}$
Channel conductivity ^c	k_c	0.1	$\text{m}^{3/2} \text{kg}^{-1/2}$
Glen’s n	n	3	
Ice flow constant cavities	\tilde{A}	5×10^{-25}	$\text{Pa}^{-n} \text{s}^{-1}$
Ice flow constant channels	\tilde{A}_c	5×10^{-25}	$\text{Pa}^{-n} \text{s}^{-1}$
Basal sliding speed	u_b	10^{-6}	m s^{-1}
Sheet width below channel ^d	l_c	2	m
Cavity spacing	l_r	2	m
Bedrock bump height	h_r	0.1	m
Englacial void ratio	e_v	10^{-3}	
Moulin cross-sectional area	A_m	10	m^2
Bed elevation	B		m
Ice thickness	H		m
Sheet input	m		m s^{-1}
Moulin input	Q_s		$\text{m}^3 \text{s}^{-1}$

^aFirst section lists physical constants, second section lists model parameters, some of which may be spatially varying, and third section lists spatially varying model inputs.

^bThe stated units are for $\alpha = 5/4$, $\beta = 3/2$, in general $\text{m}^{2\beta-\alpha} \text{s}^{2\beta-3} \text{kg}^{1-\beta}$.

^cThe stated units are for $\alpha_c = 5/4$, $\beta_c = 3/2$, in general $\text{m}^{2\beta_c-2\alpha_c+1} \text{s}^{2\beta_c-3} \text{kg}^{1-\beta_c}$.

^dThis contributes to channel melt.

therefore builds on the earlier models of Schoof [2010] and Hewitt [2011], combining the ability of the former to describe a channelized drainage system, with the continuum formulation of the distributed system of the latter. The usage of an unstructured mesh allows channels to form without directional bias, yielding what we believe is a truer representation of the real system than what is possible with a structured grid as in Schoof [2010] and Hewitt [2013]. The sheet description of the distributed system allows for simulations on larger domains than is possible with a purely network-based model. We also add an englacial storage component, as well as input to moulins that route the water to the bed at localized points [cf. Schoof, 2010]. This type of hydrology model allows for a two-way coupling to an ice-flow model through effective pressure and sliding speed as is demonstrated in Hewitt [2013]. The aim of the paper is to introduce the model’s physics, to clearly lay out its mathematical structure, to investigate its behavior with some synthetic examples, to apply it to an alpine glacier, and to discuss the results in light of previous observational work. Readers less interested in the mathematical details should skim over section 2 and focus on the results and discussion in the sections that follow.

2. Model Description

[8] The model is posed on a two-dimensional domain Ω with boundary $\partial\Omega$, on which the glacier geometry is specified by the bed elevation $B = B(x, y)$ and the ice thickness

Table 2. Variables and Units^a

Description	Variable	Units
Hydraulic potential	ϕ	Pa
Channel discharge	Q	$\text{m}^3 \text{s}^{-1}$
Channel cross-sectional area	S	m^2
Sheet discharge	\mathbf{q}	$\text{m}^2 \text{s}^{-1}$
Sheet thickness	h	m
Time coordinate	t	s
Along edge coordinate	s	m
Normal vector	\mathbf{n}	m
Test function	θ	Pa
Englacial storage	h_e	m
Hydraulic potential of bed	ϕ_m	Pa
Overburden hydraulic potential	ϕ_0	Pa
Effective pressure	N	Pa
Cavity opening rate	w	m s^{-1}
Cavity closure rate	v	m s^{-1}
Channel dissipation	Π	W m^{-1}
Channel press-melt	Ξ	W m^{-1}
Channel closure rate	v_c	$\text{m}^2 \text{s}^{-1}$
Sheet flow beneath channel	q_c	$\text{m}^2 \text{s}^{-1}$
Water volume in moulin	V_m	m^3

^aFirst section lists dependent variables, second section lists coordinates and miscellaneous variables, third section lists variables of derived quantities.

$H = H(x, y)$. Tables 1 and 2 summarize the variables and parameters.

[9] The hydraulic potential at the bed is defined by

$$\phi = \phi_m + p_w, \quad (1)$$

with p_w the water pressure, and with the elevation potential

$$\phi_m = \rho_w g B, \quad (2)$$

in which ρ_w is the density of water and g is acceleration due to gravity. The effective pressure is defined by

$$N = p_i - p_w = \phi_0 - \phi, \quad (3)$$

with the ice overburden pressure given by $p_i = \rho_i g H$ and the overburden hydraulic potential by $\phi_0 = \phi_m + p_i$. If this model were combined with a Stokes ice flow model, p_i should be replaced by the normal stress σ_{nn} at the bed.

2.1. Sheet Model

[10] The model of the water sheet follows *Hewitt* [2011] and is a continuum description of a linked cavity drainage system. We adopt cavities as the generic description of the distributed system because their behavior appears to be broadly consistent with many field measurements of ice uplift and subglacial water pressure and their mathematical description is well established. The continuum description is reached by averaging the thickness of the discrete links and cavities over a suitably large patch of the bed, on the order of 100 m^2 , to give an average sheet thickness h . Simple parameterizations of sliding and ice creep are used to describe how the cavities, and therefore the averaged sheet thickness, evolve in time. In an averaged description the distinction between different types of distributed systems is much less clear than at a microscopic level, so although our description is most obviously applicable to hard beds, the resulting model may be appropriate for soft beds too.

[11] Conservation of water mass, assuming incompressibility and saturation, demands that

$$\frac{\partial h}{\partial t} + \nabla \cdot \mathbf{q} = m, \quad (4)$$

where h is the water sheet thickness, \mathbf{q} is the discharge, and m is a prescribed source term, representing distributed surface input as well as basal melt. The discharge is related to the gradient of the hydraulic potential through

$$\mathbf{q} = -kh^\alpha |\nabla \phi|^{\beta-2} \nabla \phi, \quad (5)$$

where k is a constant, $\alpha > 1$, and $\beta > 1$. We take $\alpha = 5/4$ and $\beta = 3/2$ which corresponds to fully turbulent flow described by the empirical Darcy-Weisbach law.

[12] The time evolution of the sheet thickness is given by

$$\frac{\partial h}{\partial t} = w - v, \quad (6)$$

for some functions w and v , which parameterize the rate of cavity opening and closing, respectively [*Walder*, 1986; *Kamb*, 1987]. The opening is due to sliding over bumps in the bed, and is related to the basal sliding speed u_b through

$$w(h) = \begin{cases} u_b(h_r - h)/l_r & \text{if } h < h_r \\ 0 & \text{otherwise,} \end{cases} \quad (7)$$

where h_r is the typical bedrock bump height and l_r the typical horizontal cavity spacing. The cavities close by viscous ice deformation which is related to the effective pressure N by

$$v(h, N) = \tilde{A}h|N|^{n-1}N, \quad (8)$$

where \tilde{A} is the rheological constant of ice multiplied by an order-one geometrical factor that depends on the shape of the cavities, and n is the exponent in Glen's law.

[13] This model of distributed drainage is certainly not the only possibility. For instance, one alternative was proposed by *Flowers and Clarke* [2002] which *Hewitt* [2013] compares to this approach. Also, within our framework, other functional relations for the opening and closing rates could be used to represent other types of distributed subglacial drainage. However, care must be taken that the opening term does not lead to unbounded localization (i.e., channelization) of the water flow as this will make the problem mathematically ill posed: the sheet becomes infinitely thick in an infinitesimally narrow region. For instance a melt opening term due to dissipation of potential energy has this property and indeed this is the process causing channelization. It has been shown by *Schoof et al.* [2012] that a linked cavity system where the links behave like mini R channels, i.e., they open by melt, is necessarily unstable and flow will either shutdown or localize/channelize. Thus, in a stable linked cavity system, the links need to open due to another process, for example, due to sliding as used in this model. To still model channelized drainage (cf. section 2.4) a melt opening term is necessary, but by restricting its action to a network of conduits, we avoid the problem above.

[14] Due to the omission of the melt term, energy is not conserved in the sheet model. However, as a dissipation dominated distributed system is unstable, it will evolve either to a sheet where sliding is the leading opening mechanism or to a channelized system, both of which this model captures.

[15] Note that we impose no restrictions on the values that the water pressure can attain. This is in contrast to the model in *Schoof et al.* [2012] and *Hewitt et al.* [2012] which assumes that an air/vapor gap forms when the pressure drops to zero, and instantaneous ice uplift occurs when pressure exceeds overburden. However, the numerical procedure used in those studies is prohibitively expensive to use in 2-D.

2.2. Englacial Storage

[16] Although the sheet can store a limited amount of water, changes in water storage can only happen on the relatively slow timescale dictated by cavity opening due to sliding (equation (7)). This is not fast enough to explain many storage phenomena observed on glaciers, such as the delay between daily maximal surface melt water input and peak proglacial discharge, so we also include a faster storage mechanism in which the volume of water stored is a function of water pressure. The stored volume per unit area of the bed, h_e , needs to be included in the mass conservation equation (4):

$$\frac{\partial h}{\partial t} + \frac{\partial h_e}{\partial t} + \nabla \cdot \mathbf{q} = m. \quad (9)$$

Specifically, we envisage that this storage occurs in an englacial aquifer with a void ratio e_v [e.g., *Clarke*, 1996; *Fountain et al.*, 2005; *Huss et al.*, 2007], for which

$$h_e(p_w) = h_e(\phi - \phi_m) = e_v \frac{\phi - \phi_m}{\rho_w g}. \quad (10)$$

2.3. Channel Model

[17] We first describe the equations governing a single channel, and then show how the channels are connected to each other and to the sheet. Channels are modeled as R channels [*Röthlisberger*, 1972; *Nye*, 1976] which close due to ice creep, just like the sheet, but enlarge due to melting. Melting is driven by dissipation of potential energy in the water flow and by changes of the pressure melting point of the ice.

[18] For a single channel, mass conservation demands

$$\frac{\partial S}{\partial t} + \frac{\partial Q}{\partial s} = \frac{\Xi - \Pi}{\rho_w L} + m_c, \quad (11)$$

where S is the channel cross-sectional area (assumed always to be filled with water), Q is the discharge, s is the horizontal coordinate along the channel, Ξ is the rate of dissipation of potential energy per unit length of channel, Π is the rate of change of sensible heat per unit length of channel due to changes in the pressure melting point, and L is the latent heat of fusion. The source term m_c represents water entering the channel from the adjacent sheet.

[19] The discharge is again related to the hydraulic potential gradient via a turbulent flow parameterization,

$$Q = -k_c S^{\alpha_c} \left| \frac{\partial \phi}{\partial s} \right|^{\beta_c - 2} \frac{\partial \phi}{\partial s}, \quad (12)$$

where k_c is a constant. As for the sheet, this is equivalent to the Darcy-Weisbach relation for our choice of the parameters $\alpha_c = 5/4$ and $\beta_c = 3/2$. For a semicircular channel k_c can be related to the Darcy-Weisbach friction factor f_r by

$$k_c^2 = \frac{8}{\rho_w f_r (2/\pi)^{1/2} (\pi + 2)}. \quad (13)$$

Note that sometimes a friction factor under the same name is used which is $f = f_r/8$. Alternatively, a Manning relation could be used instead by setting $\alpha_c = 4/3$ and $k_c^2 = [\rho_w g n'^2 (2/\pi)^{2/3} (\pi + 2)^{4/3}]^{-1}$, where n' is the Manning roughness.

[20] The time evolution of S is given by

$$\frac{\partial S}{\partial t} = \frac{\Xi - \Pi}{\rho_i L} - v_c \quad (14)$$

with opening rate $(\Xi - \Pi)/\rho_i L$ and closure rate v_c . The potential energy dissipated per unit length and time is given by

$$\Xi = \left| Q \frac{\partial \phi}{\partial s} \right| + \left| l_c q_c \frac{\partial \phi}{\partial s} \right|, \quad (15)$$

where $q_c = -kh^\alpha \left| \frac{\partial \phi}{\partial s} \right|^{\beta - 2} \frac{\partial \phi}{\partial s}$ is approximately the discharge in the sheet flowing in the direction of the channel. The first term in (15) represents the contribution from the water flowing in the channel, and the second term represents a contribution from the water flowing in a width l_c of the sheet lying underneath the channel. This second term is the dissipation that was neglected in (6); it allows for flow in the sheet to cause a channelization instability even when the channel size is initially zero, provided the flow in the sheet is sufficiently large [cf. *Hewitt et al.*, 2012]. Thus, channels can nucleate without having to impose a minimal channel size as was necessary in some previous models [e.g., *Flowers et al.*, 2004].

[21] We assume that the water is always at the pressure melting point [e.g., *Röthlisberger*, 1972; *Nye*, 1976], so changes in the water pressure must be accompanied by a corresponding amount of melting or freezing at the rate $-\Pi/\rho_i L$. This process is important, for instance, it reduces the opening rate of a level channel by a factor of 1/3, and is instrumental in glaciohydraulic supercooling [e.g., *Creys and Clarke*, 2010]. However, for water flowing down a sufficiently steep slope, it causes ice melt which in turn can lead to channelization. Thus, it is also only included in the channel and not the sheet model.

[22] The sensible heat change of the water due to this process is given by

$$\begin{aligned} \Pi &= -c_t c_w \rho_w (Q + f l_c q_c) \frac{\partial p_w}{\partial s} \\ &= -c_t c_w \rho_w (Q + f l_c q_c) \frac{\partial}{\partial s} (\phi - \phi_m), \end{aligned} \quad (16)$$

where c_t is the Clapeyron slope, c_w is the specific heat capacity of water, and where we again account for the contribution from a part of the sheet underneath the channel of width l_c , as above for Ξ . We cannot allow for the channel size to become negative, so the contribution of the sheet flow to refreezing is conditional on the switch

$$f = \begin{cases} 1 & \text{if } S > 0 \text{ or } q_c \frac{\partial p_w}{\partial s} > 0 \\ 0 & \text{otherwise.} \end{cases} \quad (17)$$

[23] Finally, the closure rate of the channel due to viscous creep is

$$v_c(S, N) = \tilde{A}_c S |N|^{m-1} N. \quad (18)$$

where \tilde{A}_c is the rheological constant for ice multiplied by an order-one factor that depends on the cross-sectional geometry of the channel. The geometrical factor for the channels

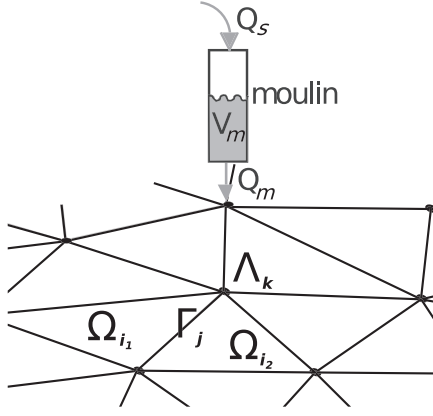


Figure 1. A view of part of a network Γ with a moulin connecting to one of the nodes. The network has edges Γ_j and nodes Λ_k , partitioning the domain Ω into subdomains Ω_i . The channels are constrained to lie on the edges and the sheet occupies the subdomains. The moulin has Q_s surface water input, Q_m discharge into network node, and a volume V_m .

is probably different from the one included in \tilde{A} used for the sheet; however, we use the same value for lack of more detailed knowledge.

2.4. Channel Network

[24] The arrangement of channel segments to form a network closely follows the model of *Schoof* [2010], but additionally, the exchange of water with the sheet has to be accounted for. Channel segments Γ_j are arranged into a network Γ , which partitions the whole domain Ω into subdomains Ω_i as depicted in Figure 1. The channels intersect and exchange water with each other at the network nodes, Λ_k , and exchange water along their length with the sheet in the adjacent subdomains Ω_{i_1} and Ω_{i_2} . The water pressure is assumed to be the same in the channels and the adjacent sheet.

[25] We use the term (*channel*) *network* exclusively to refer to Γ . The term *channel system* will be used to describe the subset of Γ on which channels of appreciable size have formed. Finally, we reserve the word *mesh* to refer to the partitioning of the domain used for the numerical discretization. In our numerics the edges of the mesh are identical to Γ ; however, implementations where Γ is a subset of the mesh edges are also feasible.

[26] Water conservation at each of the network nodes requires that the discharge flowing into the node from the channels must sum to zero (provided there is no other inflow into the node), i.e.,

$$\sum_j Q_j^k = 0, \quad (19)$$

where Q_j^k is the discharge in channel j flowing into node k , and the sum is over all channels connected to that node. Similarly, the channel source term m_c must balance the flow of water out of the adjacent sheet, so

$$m_c = \mathbf{q} \cdot \mathbf{n}|_{\partial\Omega_{i_1}} + \mathbf{q} \cdot \mathbf{n}|_{\partial\Omega_{i_2}}, \quad (20)$$

for each channel, where \mathbf{n} is the normal to the channel edge.

2.5. Moulins

[27] A significant proportion of surface melt water can enter the glacier through moulins which may deliver water directly to the channelized drainage system. This process is included in the model by connecting cylindrically shaped moulins to some of the nodes of the channel network (Figure 1). Mass conservation at these network nodes is therefore modified to

$$\sum_j Q_j^k = -Q_m^k, \quad (21)$$

where Q_m^k is the discharge out of the moulin into the channel network. As well as conducting the surface input to the bed, moulins can also store a volume of water that depends on the subglacial water pressure $V_m = V_m(p_w)$ [Clarke, 1996]. We use a linear relation for V_m ,

$$V_m(p_w) = A_m \frac{p_w}{\rho_w g} = A_m \frac{\phi - \phi_m}{\rho_w g}, \quad (22)$$

where A_m is the cross-sectional area of the moulin. This type of relation was shown by *Werder et al.* [2010b] to be consistent with tracer-experiment data. Thus, the discharge out of each moulin is

$$Q_m = -\frac{\partial V_m}{\partial t} + Q_s = -\frac{A_m}{\rho_w g} \frac{\partial \phi}{\partial t} + Q_s, \quad (23)$$

where Q_s is the (prescribed) rate of surface water input.

2.6. Summary of the Model Equations

[28] On each subdomain Ω_i , the sheet equations apply which are obtained by combining (6), (9), and (10) to give

$$\frac{e_v}{\rho_w g} \frac{\partial \phi}{\partial t} + \nabla \cdot \mathbf{q} + w - v - m = 0, \quad (24)$$

$$\frac{\partial h}{\partial t} = w - v, \quad (25)$$

where $\mathbf{q}(h, \nabla \phi)$ is given by (5), $w(h)$ by (7), and $v(h, N)$ by (8). The first equation is a parabolic equation for ϕ (if there is no storage, i.e., $e_v = 0$, it becomes elliptic), while the second governs the time evolution of h in a purely local fashion (i.e., no spatial derivatives of h are present).

[29] The sheet subdomains are separated by channel edges Γ_j on which the channel equations apply which result from combining equations (11), (12), and (14) to give

$$\frac{\partial Q}{\partial s} + \frac{\Xi - \Pi}{L} \left(\frac{1}{\rho_i} - \frac{1}{\rho_w} \right) - v_c - m_c = 0, \quad (26)$$

$$\frac{\partial S}{\partial t} = \frac{\Xi - \Pi}{\rho_i L} - v_c, \quad (27)$$

where $Q(S, \partial \phi / \partial s)$ is given by (12), $\Xi(S, h, \partial \phi / \partial s)$, by (15), $\Pi(S, h, \partial \phi / \partial s)$ by (16), and $v_c(S, N)$ by (18). The first equation is an elliptic equation for ϕ , while the second governs the time evolution of S in again a purely local fashion (i.e., no spatial derivatives of S are present).

[30] The channels are assembled into a network by enforcing water conservation at the nodes, where input from moulin can also occur (equation (21)). Finally, the channel network and sheet subdomains are all coupled via the mass exchange equation (20).

2.7. Boundary Conditions

[31] Boundary conditions on ϕ must be applied around the domain boundary $\partial\Omega$. Conversely, h and S do not require any boundary conditions as their evolution equations, (25) and (27), do not contain their spatial derivatives. The physically relevant boundary conditions are either a prescribed pressure or a prescribed water flux, both of which can be expressed as conditions on the hydraulic potential ϕ . Thus, a portion $\partial\Omega_D$ of $\partial\Omega$ has pressure (i.e., Dirichlet) boundary conditions (usually atmospheric pressure)

$$\phi = \phi_D \quad \text{on} \quad \partial\Omega_D, \quad (28)$$

corresponding to a specific potential ϕ_D , while a portion $\partial\Omega_N$ has a Neumann boundary condition

$$\frac{\partial\phi}{\partial n} = \Psi_N \quad \text{on} \quad \partial\Omega_N, \quad (29)$$

which corresponds to a specific discharge

$$q_N = -kh^\alpha |\nabla\phi|^{\beta-2} \Psi_N. \quad (30)$$

We do not allow channels to cross the boundary and thus no analogous flux conditions for them exist. If a prescribed channel inflow (or outflow) at a boundary is desired, it can be achieved through the term Q_m , i.e., using the same mechanism as for moulin inflow.

[32] Typically, boundaries where outflow occurs have a Dirichlet boundary condition at which atmospheric pressure is applied, and ‘‘upstream’’ boundaries where inflow occurs have a Neumann boundary condition at which the inflow (often zero) is prescribed. Applying pressure boundary conditions where outflow is expected can sometimes lead to an unintended pressure-driven inflow and care must be taken to ensure the correct physical condition is enforced.

2.8. Weak Formulation

[33] A convenient way to solve the coupled model equations for ϕ is to write them in weak form [cf. *Hewitt et al.*, 2012]; this enables the awkward coupling exchange terms to be dealt with naturally and automatically (see, e.g., *Elman et al.* [2005] for an explanation of weak forms in the context of finite elements, which we use for the numerics). For each sheet subdomain Ω_i , we multiply (24) by a test function θ . Integrating by parts then gives, for each Ω_i ,

$$\int_{\Omega_i} \left[\theta \frac{e_v}{\rho_w g} \frac{\partial\phi}{\partial t} - \nabla\theta \cdot \mathbf{q} + \theta (w - v - m) \right] d\Omega + \int_{\partial\Omega_i} \theta \mathbf{q} \cdot \mathbf{n} |_{\partial\Omega_i} d\Gamma = 0, \quad (31)$$

where \mathbf{n} is the outward normal to the subdomain (and also normal to the corresponding channel edges).

[34] Similarly, multiplying the channel equation (26) by θ and integrating by parts over each of the channel segments Γ_j gives

$$\int_{\Gamma_j} \left[-\frac{\partial\theta}{\partial s} Q + \theta \left(\frac{\Xi - \Pi}{L} \left(\frac{1}{\rho_i} - \frac{1}{\rho_w} \right) - v_c - m_c \right) \right] d\Gamma + [\theta Q_j]_{-}^{+} = 0, \quad (32)$$

where $[\]^{\pm}$ represents evaluation at the two ends of Γ_j .

[35] Summing these two expressions for all sheet subdomains and channel edges amounts to an integral over the

whole domain Ω . In performing this sum, notice that apart from the exterior boundaries $\partial\Omega$, each $\partial\Omega_i$ is a collection of channel segments Γ_j , so the boundary terms in (31) can be rewritten as integrals along Γ_j and around the outer boundary $\partial\Omega$. The result is

$$\begin{aligned} & \sum_{i=1}^{n_\Omega} \int_{\Omega_i} \left[\theta \frac{e_v}{\rho_w g} \frac{\partial\phi}{\partial t} - \nabla\theta \cdot \mathbf{q} + \theta (w - v - m) \right] d\Omega \\ & + \sum_{j=1}^{n_\Gamma} \int_{\Gamma_j} \theta \left[\mathbf{q} \cdot \mathbf{n} |_{\partial\Omega_{i_1}} + \mathbf{q} \cdot \mathbf{n} |_{\partial\Omega_{i_2}} - m_c \right] d\Gamma \\ & + \int_{\partial\Omega} \theta \mathbf{q} \cdot \mathbf{n} d\Gamma \\ & + \sum_{j=1}^{n_\Gamma} \int_{\Gamma_j} \left[-\frac{\partial\theta}{\partial s} Q + \theta \left(\frac{\Xi - \Pi}{L} \left(\frac{1}{\rho_i} - \frac{1}{\rho_w} \right) - v_c \right) \right] d\Gamma \\ & + \sum_{k=1}^{n_\Lambda} \sum_{j=1}^{n_\Gamma} \theta Q_j^k = 0, \end{aligned}$$

where n_Ω , n_Γ , and n_Λ are the number of subdomains, edges not on $\partial\Omega$, and nodes. Note that, unlike in standard weak forms used for finite element formulations, we integrate and sum over all edges of the mesh and not just the ones lying on the boundary.

[36] However, the definition of the channel source m_c as the exchange with the sheet, cf. (20), means that the terms in the second sum all vanish. The conservation conditions at the network nodes (21) mean that the final sums also vanish, except at moulin nodes. Moreover, the test function θ is required to satisfy homogenous boundary conditions (i.e., $\theta = 0$) on the Dirichlet parts of the outer boundary $\partial\Omega_D$, and the discharge q_N is prescribed on the remaining part $\partial\Omega_N$. Thus, we have

$$\begin{aligned} & \sum_i \int_{\Omega_i} \left[\theta \frac{e_v}{\rho_w g} \frac{\partial\phi}{\partial t} - \nabla\theta \cdot \mathbf{q} + \theta (w - v - m) \right] d\Omega \\ & + \sum_j \int_{\Gamma_j} \left[-\frac{\partial\theta}{\partial s} Q + \theta \left(\frac{\Xi - \Pi}{L} \left(\frac{1}{\rho_i} - \frac{1}{\rho_w} \right) - v_c \right) \right] d\Gamma \\ & + \int_{\partial\Omega_N} \theta q_N d\Gamma - \sum_k \int_{\Gamma_k} \theta \left(-\frac{A_m^k}{\rho_w g} \frac{\partial\phi}{\partial t} + Q_s^k \right) = 0, \quad (33) \end{aligned}$$

where, for completeness, we recall that $\mathbf{q}(h, \nabla\phi)$, $w(h)$, and $v(h, \phi)$ are given by (5), (7), and (8), $Q(S, \partial\phi/\partial s)$, $\Xi(S, h, \partial\phi/\partial s)$, $\Pi(S, h, \partial\phi/\partial s)$, and $v_c(S, \phi)$ are given by (12), (15), (16), and (18). Combining this equation with the evolution equations (25) and (27) for h and S , completes the model.

[37] The water exchange between sheet and channels has canceled out and vanished from the weak form of the equations. It is implicitly accounted for through the assumption of continuous pressure between sheet and channels: water exchange occurs at whatever rate is needed to maintain equal pressure, and thus the solution for ϕ is such that the exchange terms sum to zero. The exchange rate can then be recovered a posteriori from the solution. This is different from some previous models in which the exchange was explicitly prescribed as a function of the pressure difference between the channel and sheet [*Flowers et al.*, 2004; *Hewitt and Fowler*, 2008], where a separate ϕ is required for each system.

Table 3. Summary of Water Sources for Synthetic Model Runs

Model Run	Water Input	Spatial Dependence	Temporal Dependence
SHEET	sheet	elevation	none
MOULINS	moulins	elevation	none
DIURNAL	moulins	elevation	diurnal
Sensitivity tests	sheet	none	none

2.9. Numerical Solution

[38] We use an irregular triangular mesh to partition the domain Ω , and use the edges of these elements to form the unstructured channel network Γ . Equation (33) can be considered a parabolic equation for ϕ , which is solved using the finite element method [e.g., *Elman et al.*, 2005]. First-order elements are used to discretize ϕ and h , while S is discretized with a constant value along each edge. The integrals in the first sum of (33), over Ω_i , are discretized in the standard way. The integrals in the second sum, over Γ_j , are unusual because, in standard partial differential equation problems, integrals along the one-dimensional edges vanish. In this problem, however, they provide an essential contribution and require the integration of derivatives along mesh edges. This is relatively straightforward to implement with piecewise linear finite elements.

[39] Time stepping is performed either with a fully implicit time step, using the MATLAB `ode15s` solver, or with an operator splitting scheme. For the latter, first the ϕ -equation (33) is stepped forward by δt with a backward Euler step; then, using the new values for ϕ , the two evolution equations (25) and (27) for h and S are advanced by δt using a forward Euler step, a second-order leapfrog step, or—if there is no storage—with the MATLAB `ode113` solver. For the first two, a simple assessment scheme is used to adapt the time step δt according to a local error estimate. The model is coded in MATLAB and the meshes are generated using Triangle [*Shewchuk*, 1996], which produces meshes with uniformly distributed edge orientations.

3. Synthetic Model Experiments

[40] We perform model experiments on a 60 km by 20 km rectangular domain with a synthetic topography comprising a flat bed ($B = 0$) and a parabolic surface profile ($H \propto \sqrt{x}$) such that the ice thickness increases from zero at $x = 0$ to 1500 m at $x = 60$ km. The scale is similar to a smaller catchment of the Greenland Ice Sheet, such as the Leverett glacier catchment of ~ 600 km² [*Bartholomew et al.*, 2012]. Zero flow is imposed on the three interior boundaries, while the water pressure is prescribed to be atmospheric at the fourth

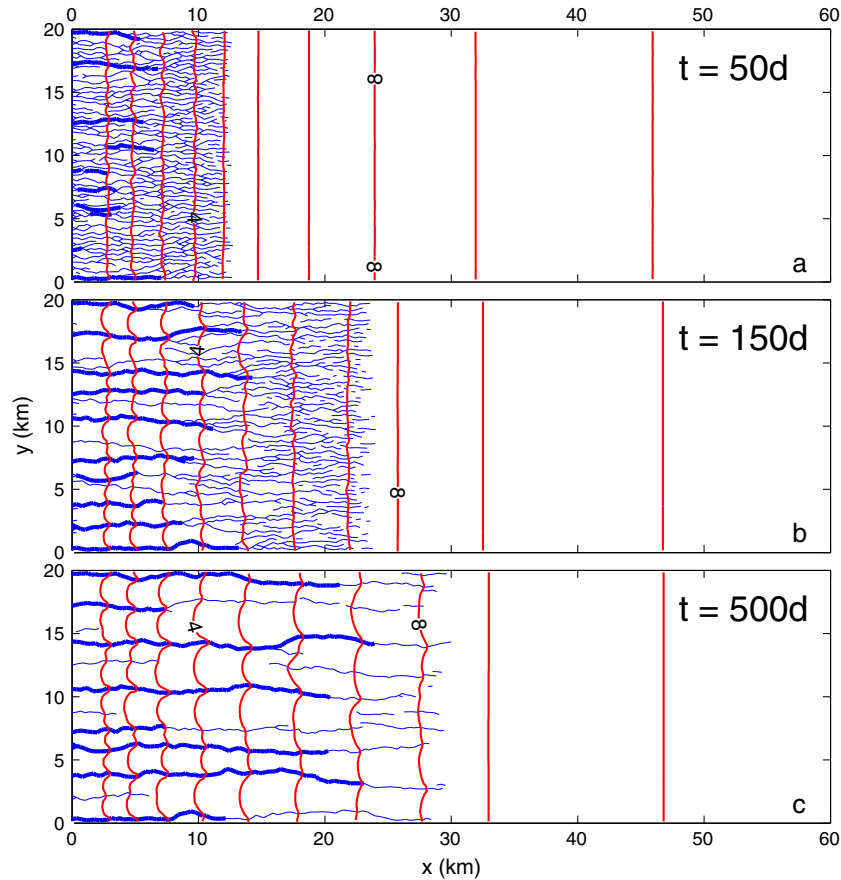


Figure 2. Time evolution of model run SHEET: map view of domain with terminus at $x = 0$ km showing snapshots of the development of the channel system at 50, 150, and 500 days with contours of the hydraulic potential (interval 1 MPa). Thick lines are plotted for larger channels ($Q \geq 20$ m³s⁻¹), and thin lines for smaller channels ($20 > Q \geq 1$ m³s⁻¹). The steady state configuration of the channel system is shown in Figure 3a.

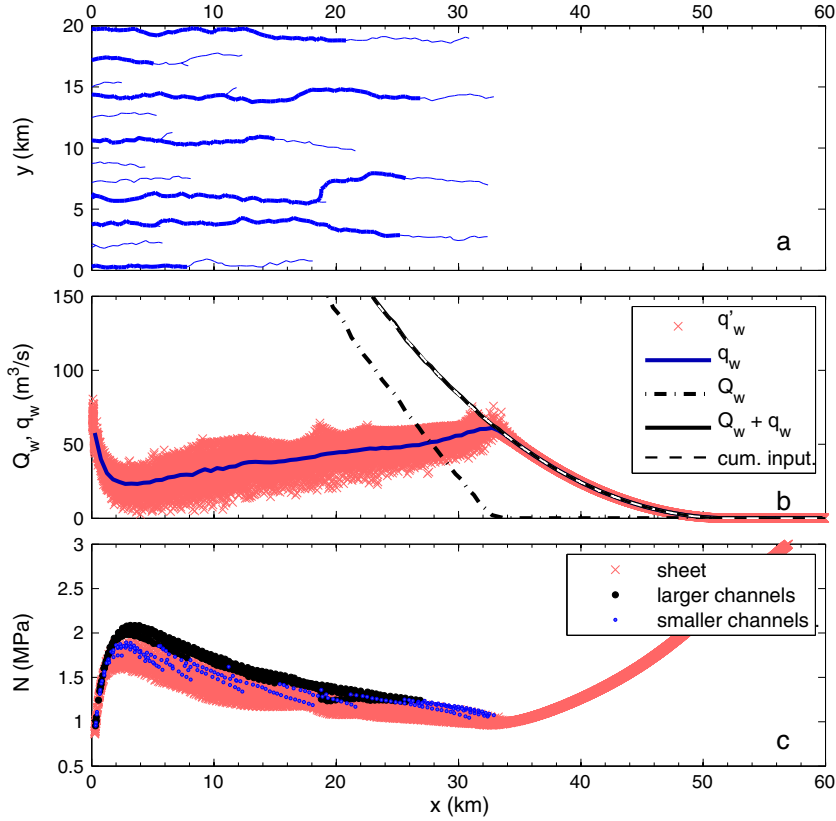


Figure 3. Steady state of model run SHEET: (a) map view of the domain with channel system with thick lines for larger channels ($Q \geq 20 \text{ m}^3 \text{ s}^{-1}$) and thin lines for smaller channels ($20 > Q \geq 1 \text{ m}^3 \text{ s}^{-1}$); (b) width-integrated quantities against distance from terminus: sheet discharge q_w (blue line), channel discharge Q_w (dash dotted), total discharge (black), total cumulative input (dashed, superimposed on total discharge), and sheet discharge on subdomains q'_w (see text for definitions); (c) effective pressure N at nodes: red crosses indicate sheet nodes, smaller blue, and larger black dots indicate nodes through which a smaller and larger channel runs. (see also Animation S1 in the supporting information).

edge ($x = 0$) corresponding to the ice margin. The different model runs are summarized in Table 3, and parameter values are given in Table 1.

[41] The three runs SHEET, MOULINS, and DIURNAL use a mesh with $\sim 10,000$ nodes and $\sim 30,000$ edges with a mean edge length of 400 m. They are forced by surface melt that varies with elevation, decreasing from 14 cm d^{-1} at zero elevation with a lapse rate of $-10 \text{ cm d}^{-1} \text{ km}^{-1}$ until it reaches 0 at $x \approx 52 \text{ km}$. This corresponds to a total input of $\sim 600 \text{ m}^3 \text{ s}^{-1}$, again chosen to be comparable to that of a smaller Greenland Ice Sheet catchment. The runs differ in how this meltwater is input into the system: in SHEET, a steady supply is fed to the distributed system (via the term m in (4)); in MOULINS, the steady supply is fed into the channel nodes through 50 moulins (via the term Q_s in (23)); and in DIURNAL, the same moulin input is modulated by a sinusoidal diurnal variation. In addition to the surface input, all model runs include a small uniform input into the sheet of 1 mm a^{-1} intended to represent basal melt.

[42] After briefly illustrating the time evolution leading to the steady state of SHEET, we concentrate primarily on the steady states themselves, or on the periodic state in the case of DIURNAL. For SHEET and MOULINS, the

simulations are run for 4000 and 8000 days (after ~ 500 days changes are only minor) starting with an initial condition of a uniformly thick sheet ($h = 0.05 \text{ m}$) and zero channel cross-sectional area; for DIURNAL, we take the final state of MOULINS and run for 50 diurnal cycles, presenting the results from the last of those cycles. In the supporting information, we provide animations of most of the figures showing the time evolution into the steady state or under the periodic forcing.

[43] The influence of different random networks on the steady state channel system is investigated by running MOULINS with three different random meshes with ~ 4000 nodes. Finally, we explore the parameter dependence of the model with several runs with all parameters but the examined one at their defaults. These runs are performed using the same domain but a spatially uniform input and a mesh with ~ 4000 nodes.

[44] Channels are allowed to form on all edges of the mesh but only few will attain an appreciable size. To visualize the channel system, we assign a threshold discharge $Q = 1 \text{ m}^3 \text{ s}^{-1}$ above which we classify an edge as a “channel” and plot it in the figures. This threshold is arbitrary, however, the steady state channel system is almost invariant for any threshold in the range $0.003\text{--}1 \text{ m}^3 \text{ s}^{-1}$.

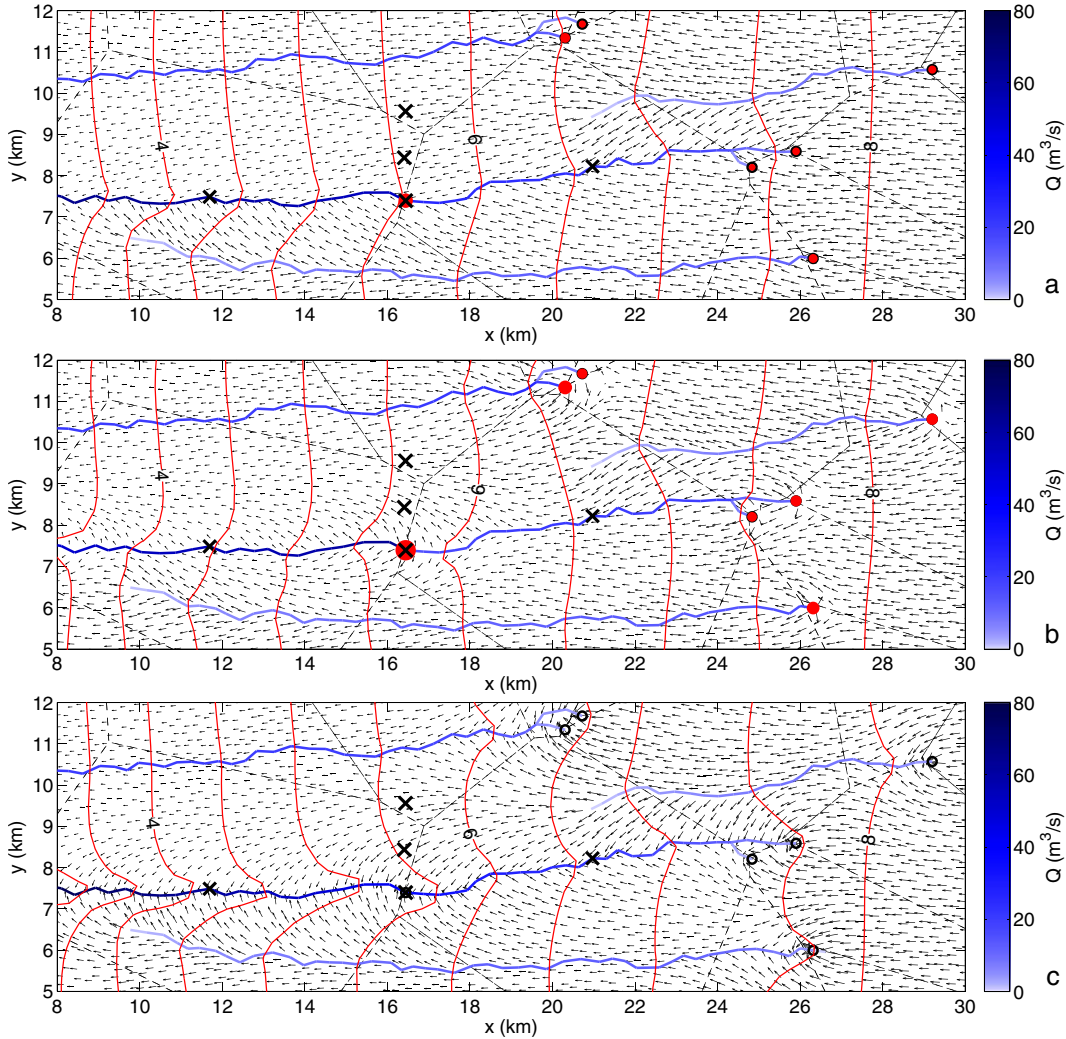


Figure 4. Model runs MOULINS and DIURNAL: Map views of part of the domain showing channel discharge Q (blue lines), sheet-flow q direction and magnitude (arrows), contours of hydraulic potential ϕ (red lines, interval 0.5 MPa), surface catchment delineations (black dashed), moulins (location black circle; water input scales with red dot size), and location of virtual experiments (crosses, cf. Figure 8). (a) MOULINS (which is very nearly identical to the diurnal average of run DIURNAL); (b) DIURNAL at midday; and (c) DIURNAL at midnight. (see also Animation S2 for MOULINS and Animation S3 for DIURNAL).

3.1. Channel System Development: SHEET

[45] Figure 2 shows how the channel system evolves for the model run SHEET from the channel-free initial state. At first, channels grow on all of the network edges roughly aligned with the water flow (cf. equation (15)) near the ice margin ($x = 0$) where the discharge is largest (Figure 2a). Major channels have formed after 150 days in the lowermost 10 km by capturing the discharge of the smaller ones, which disappear. The randomness provided by the unstructured mesh gives rise to the necessary perturbation to initialize this process. At 500 days, the channel system has nearly reached its steady state (cf. steady state in Figure 3a). However, minor rearrangements of channels still occur after more than 1000 days. Channelization causes the large-scale subglacial water pressure to drop. For instance, the 8 MPa contour moves about 4 km upstream, whereas the unchannelized region experiences almost no pressure drop.

A channel influences the water pressure locally by carving a “valley” into the potential ϕ . Thus channels divert the sheet water-flow, which is perpendicular to the ϕ contours, toward them.

3.2. Steady State With Distributed Input: SHEET

[46] In the steady state of model run SHEET, there are four major channels reaching up to ~ 32 km, beyond where there is only sheet flow (Figure 3a). Additional smaller channels begin closer to the margin between these main ones, and at the terminus there is a total of 11 channels spaced ~ 2 km apart.

[47] The channel system is only slightly arborescent, with smaller intervening channels preferentially continuing straight down the main surface gradient rather than feeding into the neighboring channels as tributaries. This is because the pressure drawdown of channels is relatively small

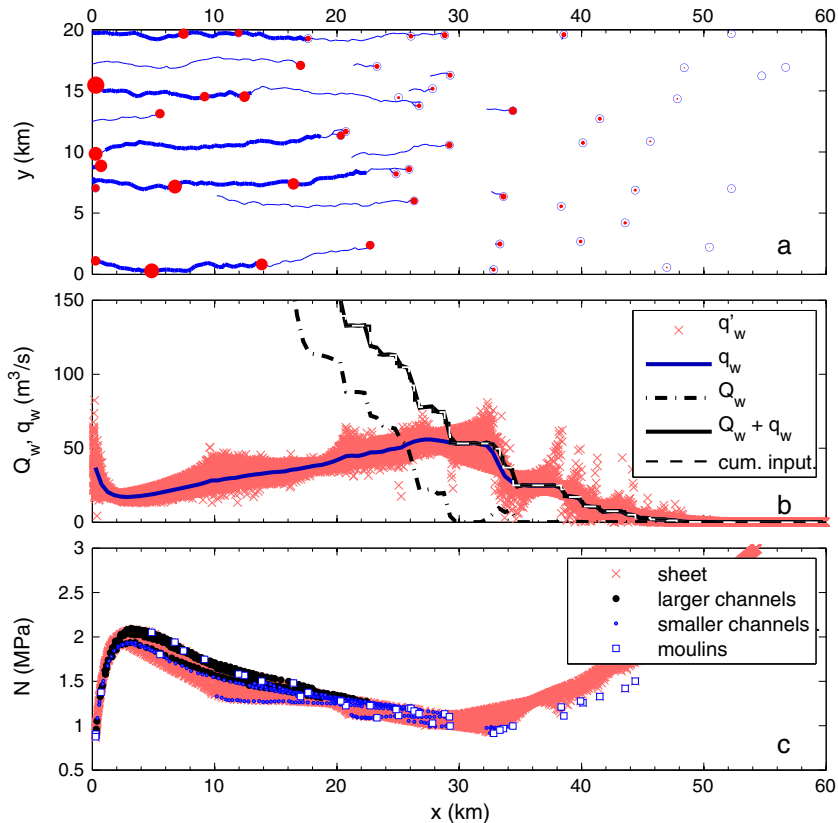


Figure 5. Model run MOULINS: layout as in Figure 3 with Figure 5a also showing moulin location (blue circle) and water input (red dot, area scales with amount); Figure 5c shows empty blue squares plotted for moulin nodes. (see also Animation S4).

compared to the background hydraulic gradient dictated by the surface slope (cf. Figure 2c). Indeed, channel branching occurs where the main channel deviates from the downslope direction, so that the tributary channel does not have to approach too obliquely.

[48] Figure 3b shows various discharge quantities across the width of the domain: the channel discharge Q_w is the sum of discharge from all channels intersecting a particular cross section, and the sheet discharge q_w is the width integral of the x component of \mathbf{q} . Also shown are the individual contributions to q_w from each of the sheet elements, q'_w , multiplied by the domain width. The scatter of q'_w in the channelized region is due to the water being captured and diverted in regions of the sheet close to channels and thus both magnitude and direction of \mathbf{q} vary.

[49] A maximum sheet discharge q_w of around $60 \text{ m}^3 \text{ s}^{-1}$ is reached where the major channels start, downglacier of which the water is transferred increasingly into the channels. Very near the terminus, q_w increases again as the thin ice limits creep closure and increases the sheet’s capacity, causing channels to leak a fraction of their water into the sheet [cf. Schoof, 2010; Hewitt, 2011]. Total water input and total discharge are equal across all cross sections, demonstrating that the model conserves mass.

[50] Where there is only sheet flow, N decreases with increasing discharge (Figure 3c); it reaches a minimum at the transition to channelized flow at $\sim 32 \text{ km}$ and then increases again, before finally dropping near the terminus due to the boundary condition imposing atmospheric pressure at

$x = 0$. This behavior is consistent with the usual expectation of steady state drainage: effective pressure decreases with increasing discharge when distributed flow prevails, and increases with increasing discharge when channelized flow prevails.

[51] At any cross section in the channelized region, N has a wide scatter. It is higher in the larger channels (black dots) than in smaller channels (blue dots) and even lower in the intervening sheet (red dots), showing that the channels create potential “valleys,” with intervening high-pressure “ridges.” The pressure difference between valley and ridges is not particularly large, consequently, the potential gradient remains predominantly in the downslope direction, and thus, as stated above, the network is only slightly arborescent.

3.3. Steady States With Moulin Input: MOULINS

[52] In the MOULINS run, the surface input is fed into 50 moulins instead of into the sheet directly. Catchment basins on the ice surface are generated by a Voronoi tessellation of randomly chosen points, and the moulins are chosen to sit at the lowest node contained within each Voronoi cell (Figure 4). The input to each moulin is then taken as the integral of the surface melt over its Voronoi cell. This approach crudely mimics the surface and englacial routing that occurs in reality, which is governed by finer details of the surface topography and the location of streams, moulins, supraglacial lakes, and crevasses [e.g., Banwell et al., 2012; Clason et al., 2012].

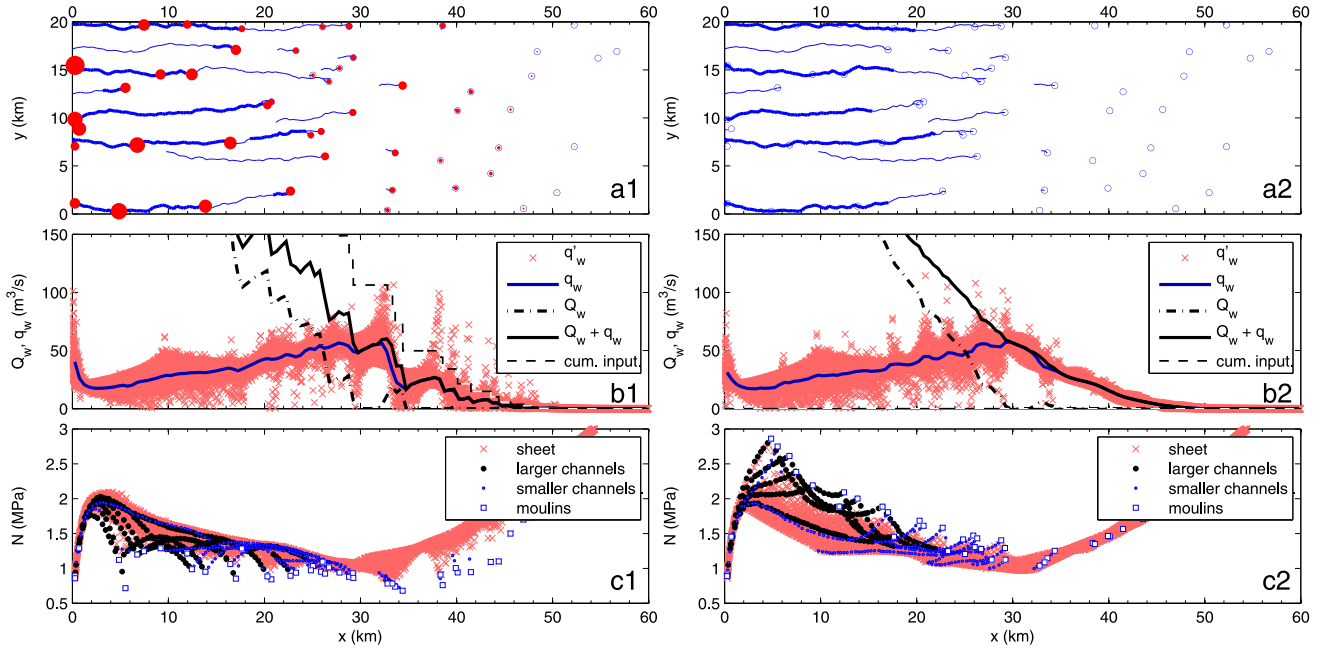


Figure 6. Model run DIURNAL: (left column, a1–c1) state of system at highest input (midday) and (right column, a2–c2) state of system at lowest input (midnight), panels are described as in Figure 3. The average over a diurnal cycle is very nearly identical to the results in Figure 5. (see also Animation S5).

[53] Subglacial channels nucleate at moulin locations and tend to link moulines that are approximately aligned in the downslope direction (Figure 5a). At the terminus there are seven channels, compared to 11 for SHEET. Continuous channels do not extend quite as far up glacier as in the SHEET run due to the fact the catchment areas of the moulines extend above them but not below. In the upper regions where sheet flow prevails, the individual elements of sheet discharge q'_w are more scattered than for run SHEET, due to water spreading out into the sheet from the injection points (Figure 5b). The water pressure in the moulines in the upper parts of the domain is higher than in the surrounding sheet (Figure 5c). In contrast, nearer the terminus where larger channels have developed, the moulin and channel pressures are generally toward the lower end of the pressure envelope (i.e., the higher values of effective pressure), similar to the SHEET run.

[54] However, there are some exceptions to this, for instance, the string of low values of channel effective pressure that is visible in Figure 5c between ~ 10 km and 20 km corresponds to a “leaky” channel located around $y \sim 6$ km (Figure 5a); water from this channel slowly spreads into the sheet and is ultimately transferred to the neighboring channels. Figure 4a shows a close up of this region which includes this and another leaky channel, located along the bottom and in the top right quadrant, respectively. The sheet discharge is indeed diverging from the channels, because the channels do not sit in a pressure valley but on pressure ridges. All the leaky channels start in the transition region between sheet and channelized flow. This is indicative of their demise: the discharge from the moulin is not quite enough to maintain the channel.

3.4. Diurnally Varying Moulin Input: DIURNAL

[55] In the run DIURNAL the steady moulin input from above is replaced by a diurnal sinusoid with the same mean and with an amplitude equal to the mean. Figures 6 (left column) show the state of the drainage system at midday, when the input is chosen to be largest, and Figures 6 (right column) show the state at midnight when there is zero input. The channel system geometry is essentially constant during a diurnal discharge cycle, since the time scale for channel evolution is longer than 24 h (Figures 6a1, 6a2). The discharge carried within the channels can nevertheless change substantially (observe that the sections with thick lines carrying the larger discharge differ between midday and midnight). The most marked feature of Figure 6 is the change in channel pressure between midday and midnight. At midday, the moulines and channels are all at a higher pressure than the sheet, so act as a source driving water laterally outward. The total channel discharge (Figure 6b1) is therefore decreasing

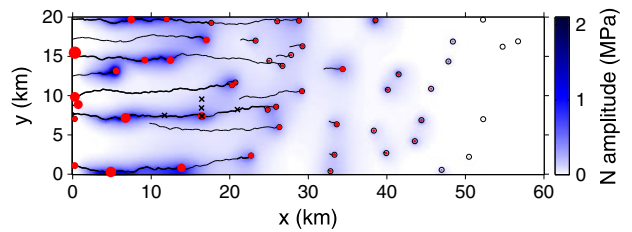


Figure 7. Model run DIURNAL: Map view of diurnal amplitude (max-min) of effective pressure (N) variation, with channels (black lines), moulin locations (black circles), moulin input (red dots scale with input at midday), and location of virtual experiments (crosses, cf. Figure 8).

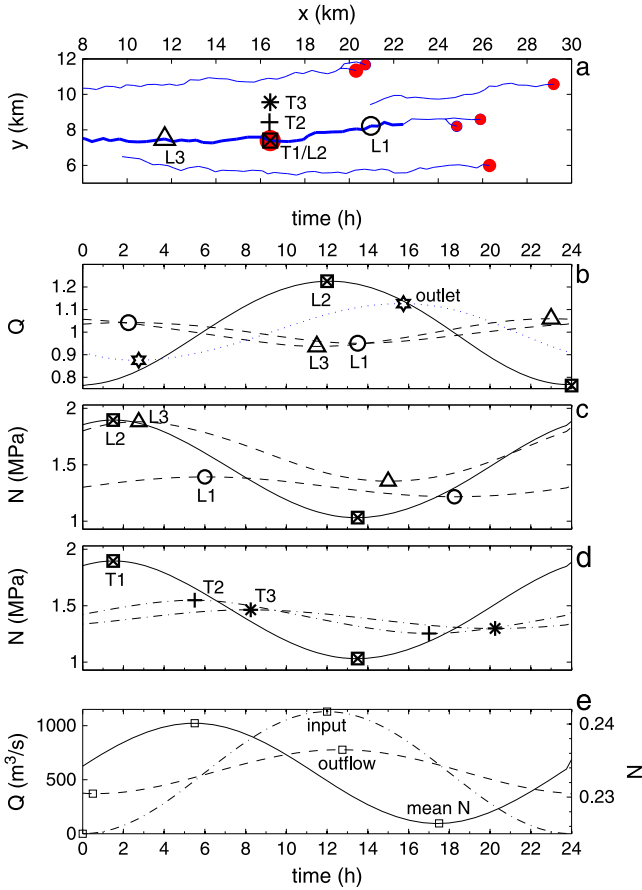


Figure 8. Model run DIURNAL: a virtual glaciological experiment of pressure and discharge measurements along a longitudinal (L1-L2-L3) and transverse (T1-T2-T3) section intersecting at T1/L2. (a) Map view of same area as in Figure 4 with channels (blue lines), moulin locations and inputs (red circles), and experiment locations (various markers; locations are also marked in Figure 4). Plots of time series with corresponding markers at their extrema: (b) Q normalized to its local mean in the channel at L1-L2-L3 and close to its proglacial outlet; (c) N at L1-L2-L3; (d) N at T1-T2-T3; and (e) total water input (dash dotted), total proglacial discharge (dashed), and mean of the effective pressure N normalized to local atmospheric pressure (solid).

downstream between the large step increases due to the water input at each moulin. In contrast, at midnight, the channels are low pressure sinks drawing the water back in from the surrounding sheet. The channel discharge then increases much more smoothly with distance downstream and is comparable to that of SHEET (Figure 3b).

[56] This contrasting behavior of channels acting as sources and sinks to the sheet is particularly evident at the moulin locations, where flow is nearly radially outward at midday and radially inward at midnight (Figures 4b, 4c). Similarly, the flow is generally away from the channels at midday and toward them at midnight, although this is somewhat dependent on the distance from the next moulin and the size of the channel. The pressure fluctuations are largest near moulins and channels. Indeed the spatial pattern of the diurnal pressure amplitude shows little variation at distances

more than ~ 2 km from these features (Figure 7). This is due to the damping effect of englacial storage setting the width over which diurnal pressure changes can diffuse, i.e., a large e_v will decrease the region with a diurnal pressure signal.

[57] To look further into spatial discharge and pressure patterns, we show time series of effective pressure and channel discharge at locations marked in Figure 8a. Figure 8d shows effective pressure at three points along the transect (T1-T2-T3) emanating from a moulin at T1. Figures 8b and 8c show the time series of the effective pressure and discharge along the longitudinal section (L1-L2-L3) centered at the same moulin. The effective pressure time series might be considered analogous to one obtained from field pressure measurements within boreholes drilled to the glacier bed.

[58] The amplitude of the pressure change along the transect (Figure 8d) decreases with distance away from the channel, as already discussed, but also incurs a progressive phase lag of up to 6 h. This behavior is reminiscent of the diffusive water pressure around a “variable pressure axis,” found by *Hubbard et al.* [1995]. The variations along the longitudinal section (Figures 8b and 8c) show a more complex pattern. The pressure at the moulin (L2) and the lower location (L3) are nearly in phase, but the upper location (L1) lags by 4 h. The channel discharge is in phase with input (cf. Figure 8e) at the moulin (L2) but in antiphase both above and below. This behavior is due to the variations of the two-dimensional flow field in the sheet and channels over the course of the day: surface input at the moulin is largest at noon and thus Q is largest then. Conversely, at the other two locations, input is also due to the inflow from the sheet which is largest at midnight (cf. Figure 4) and dominates over the discharge advected along the channel. Thus, discharge in a channel can vary both temporally and spatially in complex and surprising patterns.

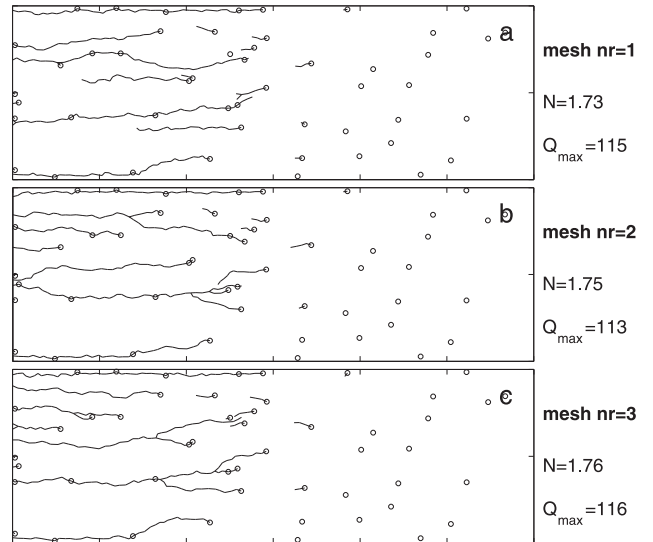


Figure 9. Channel system ($Q > 1 \text{ m}^3 \text{ s}^{-1}$) for three model runs with same parameters and inputs as for MOULINS but with different random meshes. The mean effective pressure N (MPa) and the maximal discharge of any channel Q_{max} ($\text{m}^3 \text{ s}^{-1}$) are printed beside each panel.

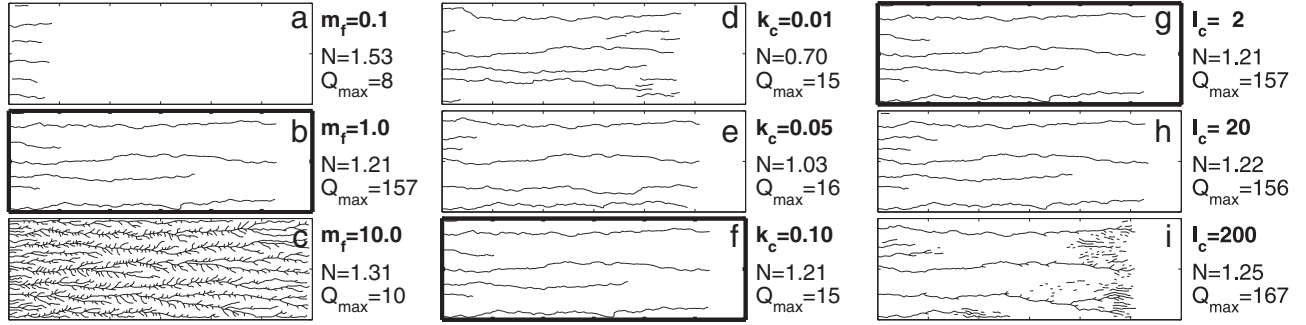


Figure 10. Channel system ($Q > 1 \text{ m}^3 \text{ s}^{-1}$) for different parameter values. Beside each panel: the varied parameter in bold, the mean effective pressure N (MPa), and the maximal discharge of any channel Q_{\max} ($\text{m}^3 \text{ s}^{-1}$). (a–c) Varying default melt input by a factor m_f ; (d–f) varying channel conductivity k_c ($\text{m}^{3/2} \text{ kg}^{-1/2}$); and (g–i) changing the width of the sheet contributing to channel melt l_c (m). The panels with thicker borders (Figures 10b, 10f, 10g) are with default parameters as given in Table 1 and thus identical.

3.5. Mesh Dependence

[59] Changing the mesh, while keeping the number of nodes constant, can produce considerable variation in the average channel spacing, in particular when using distributed input and with no topography to guide the channels, like in the model run SHEET. However, realistic topography and moulin inputs will likely introduce larger perturbations than the mesh and thus fix the channel locations in space. This hypothesis is explored by comparing three model runs with fixed moulin locations, as for the run MOULINS, but on different meshes (Figure 9).

[60] The channel system is similar between the runs with four to six major outlet channels. The domain-averaged effective pressure is the same within less than 1%, and the maximal discharge carried by any channel is within 2%. These three runs also compare well to the run MOULINS which used a finer mesh and produced five major outlet channels with $Q_{\max} = 109 \text{ m}^3 \text{ s}^{-1}$ and a mean N of 1.75 MPa. The related issue of model convergence under mesh refinement is examined in the Appendix A.

3.6. Parameter Dependencies

[61] The model contains several poorly constrained parameters, some of which also vary spatially (Table 1). The values used in the model runs SHEET, MOULINS, and DIURNAL were chosen to illustrate the general behavior of the model, and choosing other values can lead to qualitative as well as quantitative differences. We describe and explore some of the parameter dependencies, at least for steady states. To this end, we present a few suites of model runs on a mesh with ~ 4000 nodes forced with a spatially and temporally uniform input into the sheet, i.e., no moulins and no elevation dependence. As for the previous runs, the default total water input is $\sim 600 \text{ m}^3 \text{ s}^{-1}$ and the default parameters are given in Table 1. For the sensitivity experiments, we then vary a chosen parameter or input over some range.

3.6.1. Discharge and Topography

[62] Channels form when the discharge forced through the system is above a threshold depending on the model input and parameters. The channel system changes from almost nonexistent to very arborescent by varying the melt input by two orders of magnitude (Figures 10a–10c). The threshold

discharge for channelization is smaller when the topography (mostly the surface but also the bed) is steeper, since the dissipative energy available to melt the channels increases with the potential gradient. Thus, a channelized system is more likely beneath a steep alpine glacier than beneath a shallow ice sheet [Walder and Fowler, 1994; Schoof, 2010]. In our synthetic example, channels are favored closer to the ice margin both because the cumulative discharge is larger there and because the surface gradient is steeper. When channels form, their spacing tends to decrease with increasing discharge and slope, and this explains why new channels start between the existing ones close to the margin.

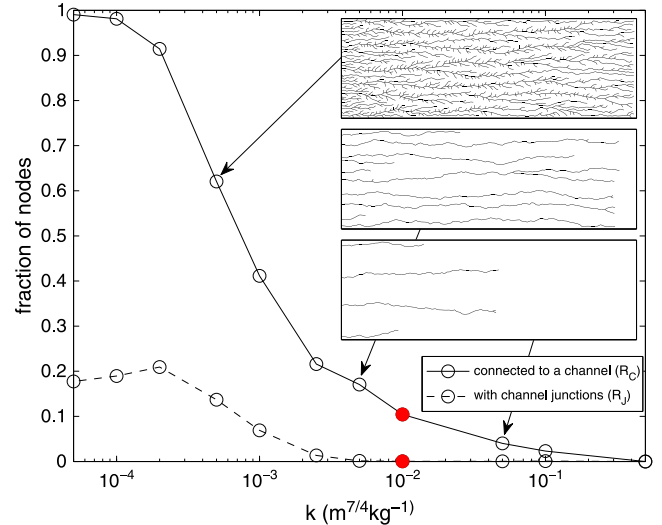


Figure 11. Density of channel system versus sheet conductivity constant k : fraction of nodes connected to a channel (R_C , solid line) and fraction of nodes with a channel junction (R_J , dashed line) versus k for an equal and uniform input into the sheet. The red dots are at the value of $k = 10^{-2} \text{ m}^{7/4} \text{ kg}^{-1/2}$ used in all other model runs. Insets show the channel system for three values of k indicated by the arrows (see also Figure S1 in supporting information for figures of the channel system for all k).

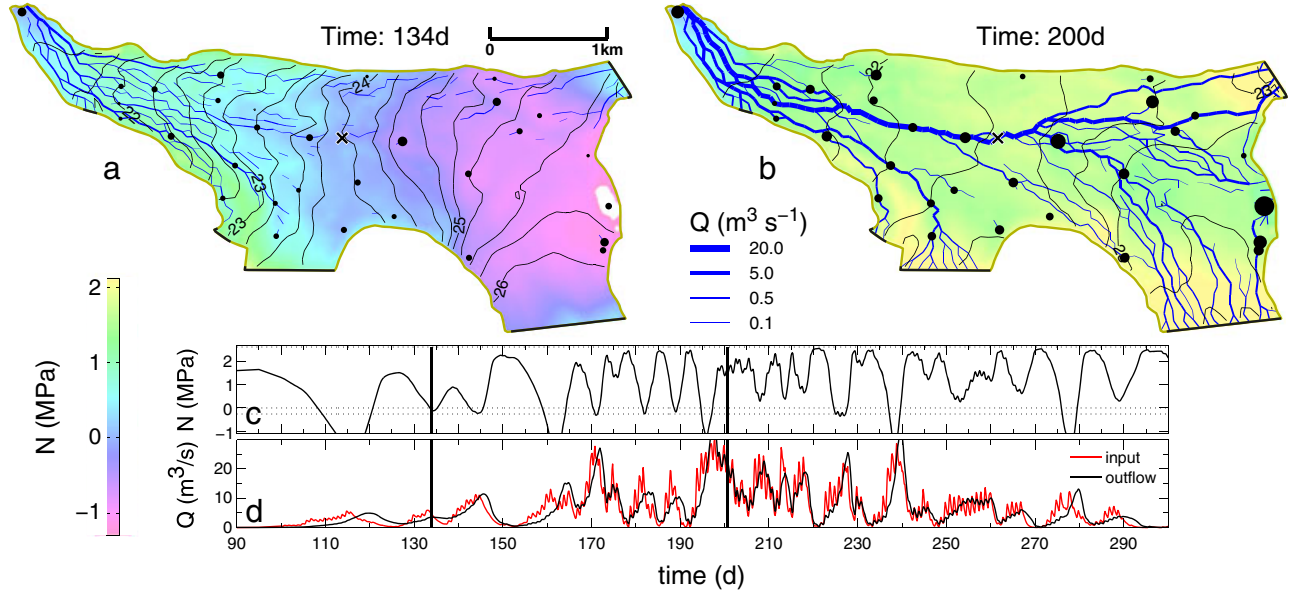


Figure 12. Simulation 2007 melt season for Gornergletscher. Snapshot of the trunk on (a) 14 May and on (b) 19 July at the time of peak input, showing contours of hydraulic potential ϕ (MPa), effective pressure N , the channel discharge Q , moulin input (dots), and inflow boundaries (black lines). (c) Time series of N at location marked by cross, with horizontal lines (from bottom) corresponding to overflow, overburden, and atmospheric pressure; (d) total input and proglacial discharge. The vertical lines indicate the time of the two snapshots. (see also Animation S6).

3.6.2. Density of Channel System

[63] For a given discharge and topography, several parameters control the relative efficiency of the distributed and channelized systems, and hence control the extent and spacing of the channels [cf. Hewitt, 2011; Schoof, 2010]. The sheet is more efficient for larger conductivity parameter k , larger bed roughness height h_r , smaller bed roughness length l_r , and faster sliding velocity u_b . Similarly, the channel is less efficient for smaller flow parameter k_c , corresponding to a rougher channel wall. All such changes act to increase the threshold discharge at which the sheet transitions to channels. A more efficient sheet also gives rise to more widely spaced channels, whereas a very inefficient sheet gives rise to a much more dense channel system.

[64] We explore the influence of the conductivity parameter k on the channel system by varying k between 5×10^{-1} and $5 \times 10^{-5} \text{ m}^{7/4} \text{ kg}^{-1/2}$. We use R_C , the fraction of nodes connected to a channel with $Q > 0.04 \text{ m}^3 \text{ s}^{-1}$, as a metric for the density of the channel system. The reason we use a lower threshold value on Q than previously is to capture even the small channels that form at low k , and thus we set the threshold to be close to the mean water input per sheet element ($0.08 \text{ m}^3 \text{ s}^{-1}$). As a measure of how arborescent the channel system is, we use R_J , the fraction of nodes that are at a channel junction, i.e., with three or more channel edges connected.

[65] At the largest k the sheet conducts water well enough that no channels at all are formed (Figure 11 and supporting information, Figure S1). As k decreases, more channels form and R_C increases until it reaches almost 1 for the lowest k . As k decreases, at first straight channels grow headward (cf. Figure 11, lowest two insets) and R_C increases

due to increased channel length and decreased channel spacing. Eventually, the channel system becomes arborescent (cf. Figure 11, top inset) until small channels reach all nodes of the mesh at the lowest k .

[66] This shift from straight channels to an arborescent channel system is reflected in R_J , which is close to zero up to the value of k that corresponds to the middle inset and then increases up to 0.2. Interestingly, the fraction R_J slightly drops for the lowest two values of k due to the shift from many small side channels, as seen in Figure 11, top inset, to longer but less branching side channels (Figure S1). This appears to be due to the strong tendency for channels to follow the ice surface gradient; at very small k the preferred arrangement is to have few long side channels running parallel to the main channels for a long distance as opposed to many small ones at more oblique angles to the x axis.

[67] The influence of the channel roughness k_c on the channel system is a bit more convoluted as illustrated in Figures 10d–10f. Decreasing k_c moves the transition between sheet and channel flow slightly downstream, as

Table 4. Parameters for Gornergletscher Run^a

Description	Para.	Value	Units
Sheet conductivity	k	5×10^{-4}	$\text{m}^{7/4} \text{ kg}^{-1/2}$
Channel conductivity	k_c	0.05	$\text{m}^{3/2} \text{ kg}^{-1/2}$
Basal sliding speed	u_b	20	m a^{-1}
Sheet width below channel ^b	l_c	10	m
Englacial void ratio	e_v	8.5×10^{-4}	
Moulin cross-sec. area	A_m	0	m^2

^aOnly parameters different from those in Table 1 are listed.

^bThis contributes to channel melt.

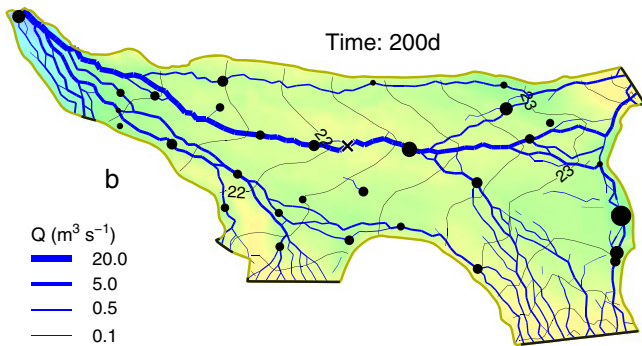


Figure 13. Gornergletscher run on 19 July with no pressure-melt term ($\Pi = 0$), layout as in Figures 12a and 12b.

argued above, and at the same time increases the channel system’s arborescence. The latter effect appears to be due to the lower effective pressure which limits creep closure of the channels and allows more of them to stay open.

3.6.3. Channel Initialization

[68] How easily a channel can begin to form is mostly influenced by the width of the sheet that contributes to channel melt, l_c (cf. equation (15)). This parameter can be thought of as representing the size and spacing of individual flow paths within the cavity system. It is loosely comparable to the spacing of conduit elements in the network model of Schoof [2010]. The choice of l_c influences the behavior of small channels during their initialization, and only minimally changes the steady state configuration except for large l_c . This can be seen in Figures 10g–10i, where the variation of l_c has little effect except at $l_c = 200$ m for which the results show more small channels in the higher reaches and a somewhat different configuration lower down.

3.6.4. Discharge Parameterization

[69] The choice of suitable values for k and k_c depends on the exponents $\alpha = 5/4$, $\alpha_c = 5/4$, $\beta = 3/2$, and $\beta_c = 3/2$ used in the discharge laws (5) and (12). Our choice is motivated by turbulent parameterizations for flow through conduits and individual orifices. For the sheet, in particular, it is possible that the average behavior of flow through many cavities is better described by a different choice (in some circumstances flow may be laminar too), and a different functional dependence of the sheet conductivity on h is also possible [Flowers and Clarke, 2002; Hewitt, 2011]. Using different exponents in the power laws does not qualitatively change the behaviors described above, however.

3.6.5. Englacial Storage

[70] In a steady state, the quantity of englacial storage plays no role. It can have a large impact on the response to temporally varying input, however. Taking a larger value for the englacial void ratio e_v leads to more damped oscillations in water pressure during the diurnal variations. It also controls the extent and timing of the pressure wave decaying away from the channel; more storage confines pressure changes to a narrower band around the channel and leads to a greater phase lag. This effect can be seen in the model run DIURNAL with $e_v = 10^{-3}$, where pressure fluctuations are limited to a strip of about 4 km wide centered on the channels (Figure 7). Storage in the moulin, controlled by

the moulin area A_m , has a similar effect in damping the diurnal oscillations.

4. Application to a Real Setting

[71] We run the model on the trunk of Gornergletscher, a large Alpine valley glacier, for the time span February to November 2007. The trunk is about 4.5 km long, 1.5 km wide, and up to 400 m thick. We use surface topography [Bauder et al., 2007] derived from aerial photography and bed topography [Farinotti et al., 2009] derived from radar measurements combined with a mass-conserving bed approach. Air temperature data are converted into water input using a distributed temperature index model coupled to a linear storage model to account for surface hydrology (e.g., retention in the snowpack). The melt occurring on the tributary glaciers is fed to the trunk through inflow boundary conditions (black lines in Figure 12). On the trunk itself, the meltwater is input through 30 randomly placed moulin locations using the same scheme as in the run MOULINS. The standard model parameters in Table 1 are used except for the ones listed in Table 4.

[72] Two snapshots of the seasonal evolution of the drainage system are shown in Figure 12 together with time series of effective pressure, water input, and proglacial discharge. One is taken in spring (14 May), at a time when the drainage system is developing, and one in midsummer (19 July) when the system is well established. Both of them are at the time of maximum daily water input. An animation of the whole melt season is provided in the supporting information (Animation S6).

[73] The first snapshot shows that in spring, a small increase in melt input overwhelms the drainage system and causes negative effective pressures to prevail in the upper half of the trunk where the channel system is not yet established. The widespread, very low effective pressures are not realistic and are caused by the model not including two processes: hydraulic jacking and allowing moulin to overflow once their water level reaches the ice surface. In the lower half of the trunk, effective pressures are higher due to the nascent channel system. However, the system is in an early stage of development characterized by many parallel channels which have yet to collapse into a few dominant ones.

[74] In midsummer this collapse has occurred and the channel system is well established. It is much more arborescent than for the synthetic model runs due to the topography channeling not only the ice flow but also the water flow at the bed. Even though the input is larger than at the time of the spring snapshot, the effective pressure is much higher due to the efficient channel system.

[75] The hydraulic potential ϕ is convex in both snapshots over large areas and the channels carve no “valleys” into the potential, unlike for instance, in the run MOULINS. For comparison, we ran the same setup with the pressure-melt term Π set to zero (equation (16)) which produces a concave potential; in particular, the main channel sits in a deep, often V-shaped trough (Figure 13). The magnitude of Π is dependent on the slope of the channel: melt is enhanced for the downsloping channels connecting the flanks with the middle of the trough; conversely, melt is diminished in the level channels lying along the valley

bottom. This process is clearly visible in the spring snapshot (Figure 12a): channel segments along the whole of the northern flank have formed, whereas the channels along the thalweg have reached only halfway. Another effect is that channels on a sloping bed are often oblique to the gradient of ϕ compared to the mostly parallel channels for $\Pi = 0$. Edges are favored to become channels for which the sum of the dissipation (Ξ) and pressure-melt term is largest (equation (14)). Whereas Ξ depends on $\nabla\phi$ only, Π also depends on the bed slope $\nabla\phi_m$ and thus channels will in general be oblique to $\nabla\phi$. The combination of these two effects, which enhance the connection of the flanks to the main drainage channel, leads to the convex hydraulic potential.

5. Discussion

[76] Our model is able to corroborate a number of long-postulated features of subglacial drainage. At low input, flow remains distributed, but above a critical discharge, the flow organizes itself into a channel system [e.g., *Flowers*, 2008; *Hewitt and Fowler*, 2008; *Schoof*, 2010]. With our choice of parameters and without lateral topographical variation, the model indicates that the channel system is only mildly arborescent consisting of almost parallel channels that largely follow the ice surface gradient. The considerable arborescence found by *Schoof* [2010], in particular, in the higher reaches, was partially due to the imposed orientation of the channels at 45° to the main surface slope. Nevertheless, this difference does not alter the fundamental conclusion that the steady state effective pressure in the channelized region increases with increasing discharge downstream.

[77] Compared to *Schoof* [2010], the novelty of this model is twofold: (1) the arrangement of the channel segments on an unstructured network and (2) the continuum description of the distributed system. The former permits more freedom in the development of the channel system, although its geometry is constrained by the particular random mesh arrangement. The latter avoids the need to resolve each cavity individually and thus overcomes the resolution limitations inherent in the older model.

[78] It is perhaps worth pointing out that the prediction of long parallel channels contrasts with typical subaerial watersheds, which often have more arborescent structures. The channel system of subaerial watersheds has been simulated quite successfully with landscape evolution models [see *Tucker and Hancock*, 2010, and references therein]. For example, *Braun and Sambridge* [2012] produce arborescent channel systems from initial topographies with no lateral variation. In contrast, the channel systems of our synthetic model runs are hardly arborescent. The difference stems from the fact that subaerial streams erode the topography and thus can significantly modify the background hydraulic potential that controls their direction. An R channel can only achieve a slight pressure reduction from its surroundings which is set by the ice overburden pressure. Thus the predominant hydraulic gradient will be aligned with the surface slope. Another very notable difference is that R channels can lie on hydraulic potential ridges, leaking discharge into the sheet (Figure 4a), whereas subaerial drainage channels will

always lie along the thalweg and capture discharge from the surroundings.

[79] The leaky channels emanating from the moulins at higher elevations show that channels are not favored if the discharge and surface slope are not large enough [cf. *Schoof*, 2010]. They contradict the common notion that channelized drainage necessarily leads to lower pressures than distributed drainage, even in steady states. Borehole measurements of *Meierbachtol et al.* [2013] in Greenland show that basal water pressures are consistently high in the upper reaches of the ablation area with very small diurnal oscillations. They conclude that, there, the drainage system cannot be channelized. Our results suggest that these findings may also be consistent with a region of leaky channels that peter out before connecting up or reaching the margin. However, on a larger scale, *Schoof* [2010] finds that, for a given total discharge, the pressure averaged over the whole domain is always lower with moulin input than with distributed input.

[80] For time varying input (model run DIURNAL, Figures 6c1, 6c2), the water pressure in the channels is not always lower than in the surrounding sheet. For instance, at midday, the water pressure is highest in the channels, in particular close to the moulins. On average, however, the time varying case still has the lowest water pressures in the largest channels. In fact, the averages of the state variables (ϕ , h , S) of model run DIURNAL are almost identical to the steady state values of model run MOULINS.

[81] However, the diurnal variation of pressure may still influence the mean ice flow speed [e.g., *Schoof*, 2010]. The dependence of sliding speed u_b on the effective pressure N is likely nonlinear, with a greater sensitivity at low N [e.g., *Iken and Bindenschadler*, 1986]. Thus, using N obtained from the run DIURNAL in such a sliding law would result in a higher average u_b compared to using N from model run MOULINS. The spatial extent of the increased average u_b would roughly be limited to the spatial extent of the diurnal pressure fluctuations (Figure 7). This spatial confinement compares well to measurements from Greenland that show that late summer speedup is concentrated around main water drainage axes [*Palmer et al.*, 2011].

[82] This confinement of pressure fluctuations along certain axes has directly been measured by *Hubbard et al.* [1995]. They found that the pressure diffuses outward from what they infer to be a channel into the distributed system. The model run DIURNAL illustrates that this oscillating lateral pressure gradient drives water into and out of the sheet during high and low discharge. Measurements of *Bartholomaeus et al.* [2008] suggest that this process is occurring during outburst floods on an alpine glacier, causing the observed ice flow speed increases and changes in proglacial meltwater composition.

5.1. Shortcomings and Modeling Issues

[83] One of the limitations of this model is that it may not cope well with sudden inputs of water and with low water pressures. In the first case, the sheet and channels are not able to expand fast enough to account for the input, and the model predicts large pressures, often well in excess of overburden. Such pressures are regularly observed in boreholes, so may not in themselves be a problem; but if the model predicts pervasive pressures above overburden it seems likely

that neglected physical processes such as hydraulic jacking are important [e.g., *Das et al.*, 2008]. Consideration of this scenario may be especially important if the model is to be linked to ice flow, since typical sliding laws suggest that the basal drag goes to zero when overburden pressure is reached.

[84] When a sloping bed is considered, the model may also predict that water pressure falls below atmospheric pressure, whereas in reality we would instead expect both channels and cavities to become only partially filled with water. The neglected effect of this may be largely to limit the rates of creep closure during periods of low discharge, since the model is then overpredicting the effective pressure that drives closure. Modifications along the lines of *Schoof et al.* [2012] and *Hewitt et al.* [2012] could be considered to account for both too low and high pressures (cf. section 2.1).

[85] A related point is that at low discharge, the model generally predicts low water pressures. This is inconsistent with many borehole pressure records that show higher pressures in winter than in summer. It is quite possible that large areas of the bed become cut off from the drainage system during low discharge in the winter. This is not currently included in this continuum model of the distributed drainage system, which predicts that the transmissivity of the sheet decreases but remains nonzero [e.g., *Murray and Clarke*, 1995; *Iken and Truffer*, 1997].

[86] Water pressures measured in closely spaced boreholes often show little or no correlation [e.g., *Fudge et al.*, 2008]. This suggests that the conductivity of the distributed system can be very low, in some instances so low that all drainage must essentially occur through conduits with no lateral connection. In a setting where this is the case, there may be little gain from simulating a distributed system with essentially zero conductivity and instead a strictly network based model [e.g., *Schoof*, 2010] could be used.

[87] We showed that using different random meshes with the same moulin locations on the same synthetic topography will produce somewhat different model results. In particular, the geometry of the channel system will change. However, the large scale behavior, for instance, the average effective pressure, remains nearly invariant. A more constraining topography than just moulin locations, such as a valley glacier or the surface depression of an ice-sheet outlet glacier, will decrease the variability of the channel system. We suspect that the errors introduced by mesh effects are likely small compared to errors introduced by uncertainties in parameters and other inputs.

5.2. Application to a Real Setting

[88] The model application to the 2007 melt season of Gornergletscher delivered promising results that broadly reflect our understanding of the seasonal and diurnal evolution of the drainage system of an alpine glacier [e.g., *Fountain and Walder*, 1998]. In spring, as meltwater flux increases, the distributed system becomes unstable and a channel system starts to develop. At this time, the highest water pressures are both modeled and measured, and lead to the observed episodes of fast ice flow, so called “spring events” [*Iken et al.*, 1983]. As the season progresses, the channel system grows headward resulting in generally lower water pressures. The many parallel channels, which the model forms at the beginning, compete with each other and

an arborescent system emerges. Conforming to observations, the model shows diurnal pressure variations and storage effects causing a phase delay of the proglacial discharge compared to input.

[89] So far, the influence of the pressure-melt mechanism on the glacier drainage system has been discussed mostly in connection with overdeepened beds and the resulting glaciohydraulic supercooling [e.g., *Lliboutry*, 1983; *Creys and Clarke*, 2010]. Our results show that this mechanism also has a profound effect on the subglacial drainage system even in the absence of overdeepenings. Melt enlargement in channels descending into the trough is enhanced, whereas for channels along the trough it is reduced. This decreases the lateral variation of the hydraulic potential. Furthermore, the pressure-melt mechanism leads to channels that are not parallel to the hydraulic potential gradient but deflected toward the downslope direction of the bed.

6. Conclusions

[90] We have presented GlaDS, a new glacier drainage system model that incorporates channelized and distributed subglacial drainage in two horizontal dimensions. The usefulness of the model lies in its potential to address such issues as the hazard of floods from subglacial and ice-marginal lakes [e.g., *Werder et al.*, 2010a], the effect of water routing on erosion [e.g., *Creys and Clarke*, 2010], and, most importantly, the impact of meltwater on ice dynamics [e.g., *Bartholomew et al.*, 2008; *Bartholomew et al.*, 2012]. A two-way coupling of this model to an ice flow model is possible [cf. *Hewitt*, 2013]: the effective pressure couples to the sliding speed which couples back to the cavity opening rate (equation (7)). This paper was intended to present the physics, mathematics, and simple test applications of the model to lay the ground work for such applications in the future. The results support and extend previous work on subglacial drainage:

[91] 1. In steady state, there is a transition from distributed flow at small discharge to a channelized system at larger discharge.

[92] 2. Only moulins that supply a sufficiently large discharge serve as channel nucleation points.

[93] 3. The channel system is self-organized and is only mildly arborescent for ice and bed surfaces without lateral variation; channels tend to follow the surface slope rather than being diverted toward neighboring channels, in contrast to subaerial rivers. However, running the model with real topography shows a more arborescent channel structure that is inherited from the surface and bed topography.

[94] 4. Channels generally act as low pressure axes that can capture water from the surrounding distributed system. For temporally varying inputs, this average behavior is masked by large pressure variations, driving water outward to the surrounding bed and englacial voids during high discharge and back into the channels during low discharge. This behavior may influence the spatial pattern of ice flow variability.

[95] 5. Channels can lie along pressure ridges, even in steady state. This is contrary, at least locally, to the common assumption that channelization necessarily leads to lower pressure.

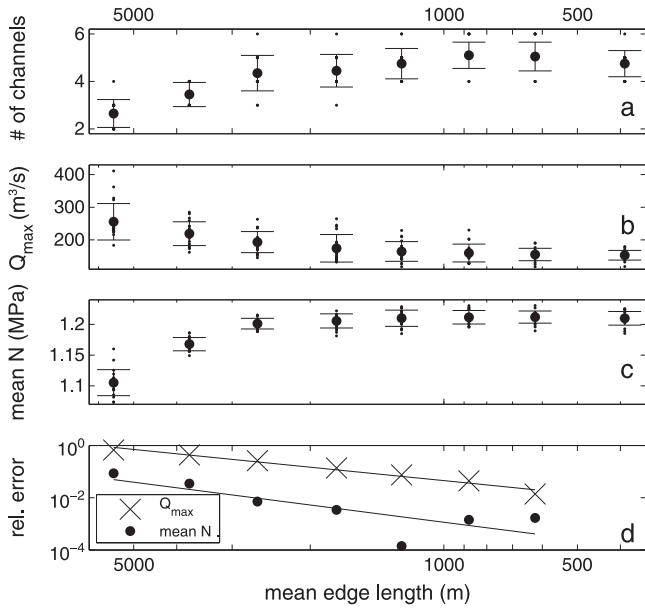


Figure A1. Dependence of three metrics on mesh size (semi-log plots): (a) The number of channels with $Q > 10 \text{ m}^3 \text{ s}^{-1}$, (b) maximal discharge of any channel, both at $x = 5 \text{ km}$, and (c) mean effective pressure over the whole domain. The small dots indicate the result from a particular random mesh, large dots indicate the average at the given resolution and the error bar gives the standard deviation. (d, log-log plot) Relative error of the averages for Q_{\max} and mean N with respect to the run with highest resolution (best fit lines have slopes of -1.7 and -2.2).

[96] 6. Pressure-melting point effects diminish the hydraulic potential variation across the trough of a glacier, as steeply dipping side channels are enlarged relative to the main channel.

[97] Not all of the model behavior is consistent with field observations. Modifications will have to be considered to include more realistic surface drainage, the effect of hydraulic jacking, open channel flow, the possible closure of drainage pathways in winter, and the erosion and transport of sediment. The model also needs to be compared quantitatively with field measurements. The ability to simulate realistic topographies demonstrated in section 4 will be crucial for this, and should enable us to constrain some of the poorly known parameters in future work.

Appendix A: Convergence Under Mesh Refinement

[98] The solution produced by a numerical scheme for solving partial differential equations should converge to the true solution under mesh refinement. However, for the presented model convergence in this sense will not be satisfied as the mesh forms part of the solution by restricting potential channel locations (cf. section 3.5). Nevertheless, convergence in some statistical sense should still be achieved for the model to be useful.

[99] To investigate this, we ran the model on the synthetic model domain using meshes with mean edge lengths between 5500 m and 400 m (corresponding to 60 to 10,000 nodes); 20 different random meshes were used at each of the

eight resolutions. As in section 3.6, the default parameters were used (Table 1) and the model was forced with a spatially and temporally uniform input into the sheet totaling $\sim 600 \text{ m}^3 \text{ s}^{-1}$.

[100] Figures A1a–A1c show the statistics of three metrics under mesh refinement. The mean of the three quantities does not change significantly for edge lengths smaller than $\sim 1500 \text{ m}$. The relative error of the averages of Q_{\max} and mean N relative to the value at the highest resolution show a convergence rate of approximately $\mathcal{O}(\Delta x^2)$ (Figure A1d). The standard deviation does not decrease much under mesh refinement which shows that there is a natural variability in the model due to the details of the mesh. This variability should decrease further once real topography is used and is unlikely to be larger than the errors of field measurements.

[101] **Acknowledgments.** M.A.W. was funded through a Swiss National Science Foundation fellowship (grant 127812) and through a Marie Curie fellowship (European Union Seventh Framework Programme (FP7/2007-2013), grant PIOF-GA-2010-275480). I.J.H. is grateful for a postdoctoral fellowship from the Killam Trusts. C.G.S. acknowledges funding from the Natural Sciences and Engineering Research Council of Canada through the Discovery grants program. G.E.F. is grateful for funding from the Natural Sciences and Engineering Research Council of Canada, the Canada Research Chairs Program, and Simon Fraser University. Some of the model runs were performed on the Western Canada Research Grid (Westgrid) of Compute/Calcul Canada. We would like to acknowledge that Sven P. Sigurðsson independently started developing a model very similar to the presented one (unpublished). We would like to thank two anonymous reviewers and Bob Anderson for their helpful comments and suggestions.

References

- Arnold, N., and M. Sharp (2002), Flow variability in the Scandinavian ice sheet: Modelling the coupling between ice sheet flow and hydrology, *Quat. Sci. Rev.*, *21*(4–6), 485–502.
- Banwell, A. F., N. S. Arnold, I. C. Willis, M. Tedesco, and A. P. Ahlstrom (2012), Modeling supraglacial water routing and lake filling on the Greenland Ice Sheet, *J. Geophys. Res.*, *117*, F04012, doi:10.1029/2012JF002393.
- Bartholomew, T. C., R. S. Anderson, and S. P. Anderson (2008), Response of glacier basal motion to transient water storage, *Nat. Geosci.*, *1*, 33–37.
- Bartholomew, I., P. Nienow, A. Sole, D. Mair, T. Cowton, and M. A. King (2012), Short-term variability in Greenland Ice Sheet motion forced by time-varying meltwater drainage: Implications for the relationship between subglacial drainage system behavior and ice velocity, *J. Geophys. Res.*, *117*, F03002, doi:10.1029/2011JF002220.
- Bauder, A., M. Funk, and M. Huss (2007), Ice volume changes of selected glaciers in the Swiss Alps since the end of the 19th century, *Ann. Glaciol.*, *46*, 145–149.
- Braun, J., and M. Sambridge (2012), Modelling landscape evolution on geological time scales: A new method based on irregular spatial discretization, *Basin Res.*, *9*(1), 27–52.
- Clarke, G. C. K. (1996), Lumped-elements analysis of subglacial hydraulic circuits, *J. Geophys. Res.*, *101*(B8), 17,547–17,559.
- Clason, C., D. W. Mair, D. O. Burgess, and P. W. Nienow (2012), Modelling the delivery of supraglacial meltwater to the ice/bed interface: Application to southwest Devon Ice Cap, Nunavut, Canada, *J. Glaciol.*, *58*(208), 361–374, doi:10.3189/2012JoG11J129.
- Creys, T. T., and G. C. K. Clarke (2010), Hydraulics of subglacial supercooling: Theory and simulations for clear water flows, *J. Geophys. Res.*, *115*, F03021, doi:10.1029/2009JF001417.
- Creys, T. T., and C. G. Schoof (2009), Drainage through subglacial water sheets, *J. Geophys. Res.*, *114*, F04008, doi:10.1029/2008JF001215.
- Das, S. B., I. Joughin, M. D. Behn, I. M. Howat, M. A. King, D. Lizarralde, and M. P. Bhatia (2008), Fracture propagation to the base of the Greenland ice sheet during supraglacial lake drainage, *Science*, *320*(5877), 778–781, doi:10.1126/science.1153360.
- Elman, H., D. Silvester, and A. Wathen (2005), *Finite Elements and Fast Iterative Solvers: With Applications in Incompressible Fluid Dynamics*, Oxford Univ. Press, USA.
- Farinotti, D., M. Huss, A. Bauder, and M. Funk (2009), An estimate of the glacier ice volume in the Swiss Alps, *Global Planet. Change*, *68*(3), 225–231, doi:10.1016/j.gloplacha.2009.05.004.

- Flowers, G., H. Björnsson, F. Pálsson, and G. Clarke (2004), A coupled sheet-conduit mechanism for jökulhlaup propagation, *Geophys. Res. Lett.*, *31*, L05401, doi:10.1029/2003GL019088.
- Flowers, G. E. (2008), Subglacial modulation of the hydrograph from glacierized basins, *Hydrol. Processes*, *22*, 3903–3918, doi:10.1002/hyp.7095.
- Flowers, G. E., and G. K. C. Clarke (2002), A multicomponent coupled model of glacier hydrology - I. Theory and synthetic examples, *J. Geophys. Res.*, *107*(B11), 2287, doi:10.1029/2001JB001122.
- Fountain, A. G., and J. S. Walder (1998), Water flow through temperate glaciers, *Rev. Geophys.*, *36*(3), 299–328.
- Fountain, A. G., R. W. Jacobel, R. Schlichting, and P. Jansson (2005), Fractures as the main pathways of water flow in temperate glaciers, *Nature*, *433*(7026), 618–621, doi:10.1038/nature03296.
- Fudge, T., N. F. Humphrey, J. T. Harper, and W. T. Pfeffer (2008), Diurnal fluctuations in borehole water levels: Configuration of the drainage system beneath Bench Glacier, Alaska, USA, *J. Glaciol.*, *54*(185), 297–306, doi:10.3189/002214308784886072.
- Hewitt, I. J. (2011), Modelling distributed and channelized subglacial drainage: The spacing of channels, *J. Glaciol.*, *57*(202), 302–314.
- Hewitt, I. J. (2013), Seasonal changes in ice sheet motion due to melt water lubrication, *Earth Planet. Sci. Lett.*, *371*–372, 16–25, doi:10.1016/j.epsl.2013.04.022.
- Hewitt, I. J., and A. C. Fowler (2008), Seasonal waves on glaciers, *Hydrol. Processes*, *22*(19), 3919–3930.
- Hewitt, I. J., C. Schoof, and M. A. Werder (2012), Flotation and free surface flow in a model for subglacial drainage. Part II: Channel flow, *J. Fluid Mech.*, *702*, 157–187, doi:10.1017/jfm.2012.166.
- Hoffman, M. J., G. A. Catania, T. A. Neumann, L. C. Andrews, and J. A. Rumrill (2011), Links between acceleration, melting, and supraglacial lake drainage of the western Greenland Ice Sheet, *J. Geophys. Res.*, *116*, F04035, doi:10.1029/2010JF001934.
- Hubbard, B., M. Sharp, I. C. Willis, M. K. Nielsen, and C. C. Smart (1995), Borehole water-level variations and the structure of the subglacial hydrological system of Haut Glacier d’Arolla, Valais, Switzerland, *J. Glaciol.*, *41*(139), 572–583.
- Huss, M., A. Bauder, M. Werder, M. Funk, and R. Hock (2007), Glacier-dammed lake outburst events of Gornerseelake, Switzerland, *J. Glaciol.*, *53*(181), 189–200.
- Iken, A., and R. A. Bindschadler (1986), Combined measurements of subglacial water pressure and surface velocity of Findelengletscher, Switzerland: Conclusions about drainage system and sliding mechanism, *J. Glaciol.*, *32*(110), 101–119.
- Iken, A., and M. Truffer (1997), The relationship between subglacial water pressure and velocity of Findelengletscher, Switzerland, during its advance and retreat, *J. Glaciol.*, *43*(144), 328–33.
- Iken, A., H. Röthlisberger, A. Flotron, and W. Haeblerli (1983), The uplift of Unteraargletscher at the beginning of the melt season—A consequence of water storage at the bed?, *J. Glaciol.*, *29*(101), 28–47.
- IPCC, Climate Change (2007), The physical scientific basis. Contributions of Working Group I to the Fourth Assessment Report of the Intergovernmental Panel on Climate Change, *Tech. Rep.*, WMO/UNEP, Cambridge Univ. Press.
- Iverson, N. (2012), A theory of glacial quarrying for landscape evolution models, *Geology*, *40*(8), 679–682.
- Johnson, J., and J. L. Fastook (2002), Northern Hemisphere glaciation and its sensitivity to basal melt water, *Quat. Int.*, *95*, 65–74.
- Joughin, I., S. B. Das, M. A. King, B. E. Smith, I. M. Howat, and T. Moon (2008), Seasonal speedup along the western flank of the Greenland Ice Sheet, *Science*, *320*(5877), 781–783.
- Kamb, B. (1987), Glacier surge mechanism based on linked cavity configuration of the basal water conduit system, *J. Geophys. Res.*, *92*(B9), 9083–9099.
- Kessler, M. A., and R. S. Anderson (2004), Testing a numerical glacial hydrological model using spring speed-up events and outburst floods, *Geophys. Res. Lett.*, *31*, L18503, doi:10.1029/2004GL020622.
- Le Brocq, A., A. Payne, M. Siegert, and R. Alley (2009), A subglacial water-flow model for West Antarctica, *J. Glaciol.*, *55*(193), 879–888.
- Liboutry, L. A. (1983), Modifications to the theory of intraglacial waterways for the case of subglacial ones, *J. Glaciol.*, *29*(102), 216–226.
- Meierbachtol, T., J. Harper, and N. Humphrey (2013), Basal drainage system response to increasing surface melt on the Greenland Ice Sheet, *Science*, *341*(6147), 777–779, doi:10.1126/science.1235905.
- Murray, T., and G. K. C. Clarke (1995), Black-box modeling of subglacial water system, *J. Geophys. Res.*, *100*(B7), 10,231–10,245.
- Ng, F. (2000), Canals under sediment-based ice-sheets, *Ann. Glaciol.*, *30*, 146–152.
- Nye, J. F. (1973), Water at the bed of a glacier, in Proceedings of the Cambridge Symposium 1969, pp. 189–194, IASH, nr. 95.
- Nye, J. F. (1976), Water flow in glaciers: Jökulhlaups, tunnels and veins, *J. Glaciol.*, *17*(76), 181–207.
- Palmer, S., A. Shepherd, P. Nienow, and I. Joughin (2011), Seasonal speedup of the Greenland Ice Sheet linked to routing of surface water, *Earth Planet. Sci. Lett.*, *302*(3–4), 423–428.
- Röthlisberger, H. (1972), Water pressure in intra- and subglacial channels, *J. Glaciol.*, *11*(62), 177–203.
- Schoof, C. (2010), Ice-sheet acceleration driven by melt supply variability, *Nature*, *468*(7325), 803–806.
- Schoof, C., I. J. Hewitt, and M. A. Werder (2012), Flotation and open water flow in a model for subglacial drainage. Part I: Linked cavities, *J. Fluid Mech.*, *702*, 126–156, doi:10.1017/jfm.2012.165.
- Shewchuk, J. (1996), Triangle: Engineering a 2D quality mesh generator and Delaunay triangulator, *Appl. Comput. Geom. Towards Geom. Eng.*, 203–222.
- Shoemaker, E. M. (1986), Subglacial hydrology for an ice sheet resting on a deformable aquifer, *J. Glaciol.*, *32*(110), 20–30.
- Siegert, M., J. Ellis-Evans, M. Tranter, C. Mayer, J. Petit, A. Salamatin, and J. Prisco (2001), Physical, chemical and biological processes in Lake Vostok and other Antarctic subglacial lakes, *Nature*, *414*(6864), 603–609.
- Tucker, G. E., and G. R. Hancock (2010), Modelling landscape evolution, *Earth Surf. Process. Landforms*, *35*(1), 28–50.
- Walder, J. S. (1986), Hydraulics of subglacial cavities, *J. Glaciol.*, *32*(112), 439–445.
- Walder, J. S., and A. Fowler (1994), Channelized subglacial drainage over a deformable bed, *J. Glaciol.*, *40*(134), 3–15.
- Weertman, J. (1972), General theory of water flow at the base of a glacier or ice sheet, *Rev. Geophys. Space Phys.*, *10*(1), 287–333.
- Werder, M. A., A. Bauder, M. Funk, and H. R. Keusen (2010a), Hazard assessment investigations in connection with the formation of a lake on the tongue of the Unterer Grindelwaldgletscher, Bernese Alps, Switzerland, *Nat. Hazard. Earth. Sys.*, *10*(2), 227–237.
- Werder, M. A., T. V. Schuler, and M. Funk (2010b), Short term variations of tracer transit speed on Alpine glaciers, *The Cryosphere*, *4*, 381–396, doi:10.5194/tc-4-381-2010.